Myrmecological News
ISSN 1997-3500
myrmecologicalnews.org
Myrmecol. News 33: 35-75 doi: 10.25849/myrmecol.news_033:035 26 January 2023
Original Article

Wonderfully weird: the head anatomy of the armadillo ant, *Tatuidris tatusia* (Hymenoptera: Formicidae: Agroecomyrmecinae), with evolutionary implications

Adrian Richter, Brendon E. Boudinot, Francisco Hita Garcia, Johan Billen, Evan P. Economo & Rolf G. Beutel

Abstract

Tatuidris tatusia Brown & Kempf, 1968, the armadillo ant, is a morphologically unique species found in low to high elevation forests in regions of Central and South America. It is one of only two extant representatives of the subfamily Agroecomyrmecinae, and very little is known about the biology of these ants, which are almost exclusively collected from leaf litter and have rarely been seen alive. Here, we illuminate the functional morphology and evolution of this species via detailed anatomical documentation of their exceptionally modified head. We describe and illustrate the skeletomuscular system, digestive tract, and cephalic glands based on high-resolution micro-computed tomography scan data. We hypothesize that the modifications which produce the unusual "shield-like" head shape are the result of complex optimizations for mandibular power, physical protection, and balance. The most conspicuous cephalic features are the broadening of the frontal region and foreshortening of the postgenal region. The former characteristic is likely also associated with the lateral position of the antennal scrobe, the inverted antennal articulation, and the broad attachment surface for the mandibular adductor muscles. This head geometry also comes with a degree of internal restructuring of the tentorium and the antennal musculature, which have a unique configuration among ants studied so far. The mandibular blades, and their articulations and muscles, are highly distinctive compared with previously evaluated species. Using a 3D-printed model, we were able to hypothesize their entire range of motion as the mandibles fit tightly into the oral foramen. Finally, we compare *T. tatusia* across other related subfamilies and discuss the evolution of the Agroecomyrmecinae and other species-poor and phylogenetically isolated "relictual" lineages.

Key words: Micro-computed tomography, evolutionary morphology, relictual lineage, adaptation, *Paraponera*, *Ankylomyrma*.

Received 14 February 2022; revision received 10 November 2022; accepted 10 November 2022
Subject Editors: Flávia Esteves, Florian M. Steiner

Adrian Richter (contact author), Brendon E. Boudinot & Rolf G. Beutel, Institute of Zoology and Evolutionary Research, Friedrich Schiller University Jena, Erbertstr. 1, Jena 07743, Germany, E-mail: adrichter@gmx.de

Francisco Hita Garcia, Biodiversity and Biocomplexity Unit, Okinawa Institute of Science and Technology Graduate University, Onna-son, Okinawa, 904-0495, Japan.

Johan Billen, Zoological Institute, KU Leuven, Naamsestraat 59, Box 2466, 3000 Leuven, Belgium.

Evan P. Economo, Biodiversity and Biocomplexity Unit, Okinawa Institute of Science and Technology Graduate University, Onna-son, Okinawa, 904-0495, Japan; Radcliffe Institute for Advanced Study, Harvard University, Cambridge, MA, 02138, USA.

Introduction

Tatuidris tatusia Brown & Kempf, 1968 is the "armadillo ant" in both form and name. The silhouette of these strongly armored ants is compact and profoundly curved, while both elements of the binomen refer to armadillos: The genus name is a combination of the Tupi word for the order Cingulata (*tatu*) and the Greek word for ant (*idris*), and the specific epithet is derived from a synonymized generic name for those armored mammals. This morphologically singular species was described based on two specimens from El Salvador (Quezaltepeque), which were sent to the original authors by Roy Snelling from the Los Angeles County Museum (Brown & Kempf 1968). Since that time, the number of collected specimens has considerably increased, and the known distribution range extended north to Mexico and south to Peru and Brazil (Donoso 2012, 2017).

Initially considered to be a lineage of Myrmicinae that was transitional from Ponerinae sensu lato, *Tatuidris tatusia* was placed in the tribe Agroecomyrmecini alongside the Eocene genera †*Agroecomyrmex* Wheeler, 1910 and †*Eulithomyrmex* Carpenter, 1935 (Brown & Kempf 1968). Because of its well-developed postpetiole and "dacetine"-like facies, *T. tatusia* featured prominently as a point of contention among morphological systematists and was subjected to a protracted series of back-and-forth rearrangements (Baroni Urbani & al. 1992, Baroni Urbani & de Andrade 1994, Bolton 1998, 1999, 2000, 2003, Baroni Urbani & de Andrade 2007). The disagreement was ultimately settled via the generation and analysis of molecular datasets (e.g., Brady & al. 2006, Moreau & al. 2006, Rabeling & al. 2008, Ward & al. 2015), which unambiguously supported the elevation of Agroecomyrmecini to subfamily level (Bolton 2003). These analyses, moreover, revealed that the ornate African species *Ankylomyrma coronacantha* Bolton, 1973 is sister to *T. tatusia* (see Ward & al. 2015), for which a current diagnosis was provided by Fisher & Bolton (2016). That Agroecomyrmecinae is nested within the Poneria ("poneroids") is supported by the aforementioned studies as well as more recent molecular analyses (e.g., Branstetter & al. 2017, Borowiec & al. 2019), and a sistergroup relationship between Agroecomyrmecinae and Proceratiinae, with Paraponerinae sister to both, was even more recently supported by the phylogenomic analysis of Romiguier & al. (2022).

Even half a century since its original description, the species-level diversity and natural history of *Tatuidris tatusia* remain uncertain. The occurrence of apparently distinct pilosity among forms of *T. tatusia*, differentiated by setational curvature, stature, and density, led to the hypothesis of multiple morphospecies (Longino 2010), and eventually the recognition of one form as "*Tatuidris kapasi*" Lacau & Groc, 2012 in Lacau & al. (2012). Soon thereafter, Donoso (2012) systematically evaluated the morphological and cytochrome oxidase subunit I variation of *T. tatusia* across its range, finding that the primary signal was of latitudinal variation without discrete morphological gaps and that the multiple hair forms occurred within defined sequence clusters. Donoso (2012), therefore, tentatively concluded that *T. tatusia* represents a single species in the process of allopatric differentiation, stressing that the recognition of multiple species may yet result from larger datasets and more sophisticated analyses. Recent advances in these regards have shown Donoso's foresight (2012), as complicated and morphologically subtle species boundary patterns can indeed be resolved in taxa of Formicidae using the approaches he suggested (e.g., Prebus 2021, Branstetter & Longino 2022, Ward & Branstetter 2022, Williams & al. 2022). To date, the most extensive contribution to the biology of *T. tatusia* was provided by Jacquemin & al. (2014); their field- and lab-based videos showed that *T. tatusia* ants are slow to the point of clumsiness, with an oversized head and body size exceeding that of other ant species of the Neotropical soil or leaf litter. The nitrogen stable isotope ratio analysis of those authors indicated that *T. tatusia* is likely a top predator of the brown food web (as defined by Kaspari & Yanoviak 2009), and their laboratory "cafeteria experiments" suggested that *T. tatusia* may be rather specific in their prey choice. However, the prey preference of *T. tatusia* remains a mystery as the ants rejected all offered food items.

The primary objective of the present study is to document the cephalic anatomy of this unusual ant species in detail using modern techniques, while the secondary objective is to understand the morphological evolution of *Tatuidris tatusia* in the light of recent phylogenomic advances. In addition to providing a considerably expanded and precise treatment of the external morphology of *T. tatusia*, this work expands our knowledge of the variation of internal head structures, including muscles, the cephalic digestive tract, and cephalic glands, complementing similar analyses for representatives of Formicinae, Ponerinae, Myrmicinae, Leptanillinae, Dorylinae, and †Sphecomyrminae (Richter & al. 2019, 2020, Boudinot & al. 2021, Richter & al. 2021a, 2022). We employed micro-computed tomography (μ-CT) scanning for our anatomical analysis and volume renderings to illustrate the anatomy. Furthermore, we printed a 3D model of the head capsule and mandible to investigate the unusual mandibular articulation of *T. tatusia* and the mandibular movement pattern resulting from it. Our contribution provides new information on a little-known group of ants and presents thoughts on the morphological evolution and survival of a taxonomically depauperate and phylogenetically isolated lineage, otherwise known as phylogenetic "relicts".

Material and methods

Material examined

Tatuidris tatusia (Agroecomyrmecinae): The single specimen used in this study for μ-CT scanning was collected in Costa Rica: Alajuela, 5 km east of Monteverde, 10° 17' 47.2" N, 84° 46' 16.8" W, 1230 m above sea level (a.s.l.), wet forest, ex sifted leaf litter, Winkler, collection code JTL8695-s, 18.V.2014, leg. J. Longino. After μ-CT scanning, the specimen was given the unique specimen identifier (USI) CASENT0790526 and is now stored at the research collection of the Biodiversity and Biocomplexity Unit at the Okinawa Institute of Science and Technology. The two workers used for histological examination were collected by Thibaut Delsinne in the Copalinga Private Reserve, Ecuador, 4° 5' 28.3" S, 78° 57' 38.5" W, 1050 m a.s.l., and were obtained via Winkler extraction of leaf litter samples. They are stored in the embedding database of Johan Billen at Katholieke Universiteit Leuven under numbers 2355-1 and 2355-2, with the corresponding section series kept in drawer 38C, numbers 32 to 46. Additional specimens of *T. tatusia* examined from stacked photographs or scanning electron micrographs (SEMs) are indicated in Table 1. For the purpose of comparing *T. tatusia* with other Formicidae in a phylogenetic

Fig. 1: Macrophotographs of living *Tatuidris tatusia*. Upper row: ventral view on the left and lateral view on the right. Lower row: dorsoventral view. Note the smooth, shining cuticle, inclination of the head, and the massive size of the head relative to the mesosoma and gaster. Photographs by Michael Branstetter and used with permission. Scale bars represent an estimation based on the dimensions of our 3D model.

context, we also examined specimens from Keller's (2011) SEM atlas, for which images are available on AntWeb (2022); the USIs for these specimens are listed in Table 1. USIs were not recorded for other specimens evaluated from AntWeb (2022) because of the varying taxonomic granularity of our comparisons coupled with the default display settings of AntWeb (2022) (see also "Comparative morphology" below). One *Ankylomyrma coronacantha* specimen (Ent:728292) was examined directly by AR at the Harvard Museum of Comparative Zoology in Harvard, Massachusetts.

µ-CT scanning and 3D-reconstruction

The head of the sample for µ-CT scanning was removed with forceps and stained in an alcoholic iodine solution for three days before it was mounted in a pipette tip filled with 99.9% ethanol. The images were captured with a Zeiss Xradia 510 Versa 3D X-ray microscope (Oberkochen, Germany) operated with the Zeiss Scout-and-Scan Control System software (version 11.1.6411.17883) at the Okinawa Institute of Science and Technology Graduate University, Japan. The scanning parameters chosen consisted of a 40 kV (75 µA) / 3 W beam strength with 20 s exposure time under a 4 × magnification, which resulted in a pixel image size of 1.41 µm. The distance between the sample and source was set to 13 mm and the distance to the detector to 50 mm. 3D reconstructions of the resulting scan projection data were done with the Zeiss Scout-and-Scan Control System Reconstructor (version 11.1.6411.17883) and saved in DICOM file format. Postprocessing of DICOM raw data was performed with Amira (version 6.0) software (Visage Imaging GmbH, Berlin, Germany). Individual structures

were segmented into discrete materials. For segmenting the head capsule, every 20th slice was pre-segmented in Amira, and the online platform Biomedisa (Lösel & al. 2020) was used to semiautomatically complete the segmentation. The segmented materials were then exported with the plugin script "multiExport" (Engelkes & al. 2018) in Amira (version 6.1) as Tiff image stacks. VG-Studio Max 3.4 (Volume Graphics GmbH, Heidelberg, Germany) was used to create volume renders out of the Tiff image series.

3D-printing for functional morphology

In addition to the volume renderings generated to illustrate our anatomical results, surface objects of the head capsule and mandible were generated with Amira (version 6.0) and exported as .stl files. These surface files were printed with an objet350 3D printer (Stratasys, Rehovot, Israel), using the solid, white digital acrylonitrile butadiene styrene (ABS) material. The models were used to investigate the potential mandibular movement of *Tatuidris tatusia*. A series of images of the opening movement at different angles was taken with a Huawei mate 20 lite (Huawei, Shenzhen, China) smartphone camera and is presented in the discussion section.

Histological sections

The anterior part of the head of two workers was cut off with a sharp razor blade and fixed in 2% glutaraldehyde in a sodium cacodylate buffer, followed by post-fixation in 2% osmium tetroxide in the same buffer. After dehydration in a graded acetone series, tissues were embedded in araldite (Agar Scientific Ltd, Sansted, UK) and sectioned with a Leica EM UC6 ultramicrotome (Wetzlar, Germany), one head in longitudinal and one in a transverse orientation. Semithin sections of 1 µm thickness were stained with methylene blue and thionin and examined in an Olympus BX-51 (Tokyo, Japan) microscope. With an Olympus Camedia C-3040 Zoom digital camera (Tokyo, Japan), images of histological sections were taken at 10 µm intervals using the 20 × objective, and additional images of anatomical details were taken with a 40 × objective and a 100 × objective with immersion oil with a focus on glandular features.

Image processing

All images were edited with Adobe Photoshop® CS6 (Adobe System Incorporated, San Jose, USA) and arranged into figure plates (Figs. 1 - 17). On SEM images and images from the section series, a tonal correction was performed. The selective sharpener (30% strength) was used on all images. Adobe Illustrator® CS6 (Adobe Systems Incorporated, San Jose, USA) was used to label the figure plates.

Data availability

The µ-CT scan data generated for this study were uploaded to Zenodo.org and can be accessed under the following DOI: https://doi.org/10.5281/zenodo.6046240. The Zenodo repository also contains the surface renders of the head capsule and mandible. Using this, anyone with access to a 3D printer can reproduce the mandibular movement experiments performed in this study.

Terminology

The terminology of the head and its appendages is based on Keller (2011) and Richter & al. (2020), with additions made to hypostomal and mandibular terminology from Richter & al. (2022). The names and numbers used for head muscles are based on Wipfler & al. (2011). For previous applications of this system to Formicidae and comparative muscle tables, see Richter & al. (2019: tab. 1) and Richter & al. (2021a: tab. 2). Orientational descriptors (anterior, posterior, dorsal, ventral) assume prognathy to facilitate comparison with other ant species, although the head of *Tatuidris tatusia* is typically more strongly inclined than in many other lineages (e.g., Richter & al. 2019, 2020, 2021a). Operationally, this means that the oral foramen is anterior and the vertexal area of the head is posterior while the occipital foramen is on the ventral and the frontal area on the dorsal side of the head. Terminology for surface sculpturing follows Harris (1979). The systematic terminology follows Boudinot & al. (2022a), in which the "poneroid" and "formicoid" clades are referred to as Poneria and Doryloformicia, respectively, to avoid confusion with the superfamilial rank (suffixes: nominal -oidea, adjectival -oid).

Based on the functional, morphological investigation presented here, it was necessary to derive new concepts, hence terms, that are specific to the craniomandibular articulations and associated structures of *Tatuidris tatusia*. Because of the uncertain homology of several of these structures to other groups, we prefer to use these specific terms based on functional relevance to facilitate our discussion of mandible movement. We also discuss the concepts "trulleum" and "canthellus". These new and revised concepts are listed below.

Clypeal condyle rail: the long, transversely oriented part of the cranial condyle (ccr, Fig. 2D). This rail may correspond to the triangular process of the clypeus described in other ants (see Richter & al. 2019), but that process does not interact with the mandible or function as a condyle. Alternatively, it may be a modified part of the clypeal condyle.

Clypeal condyle lobe: the short lobe of the cranial condyle perpendicularly oriented to the condyle's long part (ccl, Fig. 2D). This corresponds in position to the cranial condyle of other aculeatan species (e.g., Richter & al. 2020, 2022).

Distal contact surface: the dorsal groove on the mandibular base in which the clypeal condyle rail rests in a closed position (dcs, Fig. 4C).

Medial mandibular groove: the dorsal groove into which the clypeal condyle rail slides during mandible opening (mg, Fig. 4C, E). The medial groove is distally bordered by a short lobe, which we call the **dorsal canthellar lobe** (dcl, Fig. 4C, E). One or both of these grooves may correspond to the "**trulleum**" of Ettershank (1966),

but the homology of this structure is unclear at the moment (see below).

Lateral and **medial mandibular acetabular grooves:** the lateral ($mdag_l$, Fig. 4C) and medial ($mdag_m$, Fig. 4C) portions of the mandibular acetabulum, which receives the clypeal condyle and is generally in the form of a single groove but in *Tatuidris tatusia* is divided into two by a triangular ridge.

Fimbrial line carina: the carina (flc, Fig. 4C, E) that accompanies the line of setae along the medial surface of the masticatory margin (termed fimbrial line after Richter & al. 2022 and Michener & Fraser 1978).

Stipitopremental conjunctival thickening: the more or less sclerotized part of the conjunctivum that connects the inner side of the stipes to the prementum and hypopharynx, in distinction to the surrounding thin and flexible regions of the conjunctivum. Previously, this was referred to as the "stipitopremental conjunctivum" in Richter & al. (2020) and (2021a) and corresponds, for example, to the "conjunctival thickening" of Porto & Almeida (2019) and possibly to the "anterior conjunctival thickening" of the Hymenoptera Anatomy Ontology (HAO:0002072, e.g., used in Prentice 1998), although that definition includes a connection to the labrum.

Trulleum: The trulleum was originally defined in species of Myrmicinae with a distinct "canthellus" (see corresponding section below). The canthellus, basal mandibular margin, and proximal mandibular base together form the roughly triangular walls of the depressed trulleum (Ettershank 1966: fig. 2). However, as this specific condition is restricted to Myrmicinae (Richter & al. 2019), and mandibular grooves / depressions of various other shapes occur in some, but by no means all, Formicidae in similar positions (e.g., Richter & al. 2021b), Richter & al. (2019) suggested that use of the term should be restricted to the myrmicine condition. We follow this interpretation here, and while "trulleum" could conceivably be established as a pragmatic referral to various kinds of mandibular grooves, we would prefer this to be based on a thorough evaluation of such grooves and their homology, which is outside the scope of the current contribution. As with other terms, we choose to employ a homology-neutral term, emphasizing functional role instead (here "distal contact surface" and "medial groove", see corresponding sections above). We also suggest here a modified use of Ettershank's (1966) term "canthellus".

Canthellus: The term "canthellus", as used by Ettershank (1966), refers to the dorsal outgrowth / ridge of a medial thickening of the mandibular base. Instead, we propose to apply this term to the medial thickening as a whole as the latter appears to be widely present across Formicidae (Richter & al. 2019: fig. 4D, therein referred to as "canthellar elevation", see also Richter & al. 2020, 2021a) while the dorsal ridge is restricted to some taxa such as Myrmicinae. This usage makes the term more widely applicable across Formicidae. Because the dorsal outgrowth of the canthellus observed in *Tatuidris tatusia* is restricted to part of the overall canthellus length, we call it "canthellar lobe" here (see above). "Canthellar ridge" may be more appropriate for the condition observed in Myrmicinae.

Comparative morphology

In order to comprehend the evolutionary derivation of *Tatuidris tatusia*, we compared the external morphology of the head, mesosoma, and metasoma with a sample of other Poneria. We relied on Keller's (2011) SEM atlas for detailed comparisons of the head and on AntWeb (2022) for comparisons across the rest of the body. Additional sources of information for individual characters are indicated where necessary. Our comparative process was structured by the phylogenies of Branstetter & al. (2017), Borowiec & al. (2019), and Romiguier & al. (2022), that is, using the character concepts of Bolton (2003), Keller (2011), Boudinot (2015), and Boudinot & al. (2022a) as a basis, we iteratively compared sister-groups where reasonably supported from the species to the supra-subfamilial level in a node-spanning manner. To evaluate image arrays, we used the subfamily, genus, and species classification tool of AntWeb (2022) to view specimens of given castes and taxa side by side, with multiple cycles of higher-to-lower and lower-to-higher taxon comparison. We recorded morphological variables in Table 2 at the species level for *Tatuidris*, *Ankylomyrma*, *Paraponera*, and *Apomyrma* (given that they are currently monotypic), while our scoring for the comparatively diverse subfamilies Amblyoponinae, Ponerinae, and Proceratiinae represents a generalization across the species and genera contained therein. As evaluating patterns of morphological transformation in these three larger subfamilies is not the focus of the present study, we usually did not record variables within these clades.

The characters listed in Table 2 were coded as state arguments that are either TRUE (1) or FALSE (0), in a manner similar to Boudinot & al. (2022a) but with "0" representing the inferred plesiomorphic condition. Hypotheses of state polarities, presented in Figure 12, are based on an informal, parsimony-based evaluation informed by the ancestral state estimates of Boudinot & al. (2022a) and Richter & al. (2022). If a given structure could not be evaluated based on available images, it was recorded as "?". Overall, the coding accounts for unique as well as shared features of all scored taxa and mostly includes features that are externally visible; internal observations were restricted to *Tatuidris tatusia* and are considered comparatively ambiguous.

We note that the resultant table of variables is not specifically intended for statistical phylogenetic analysis. Rather, the table is intended as a summary of possible morphological transformations. Given their distribution across the focal taxa, these transformations may be reasonably hypothesized to have evolved along particular branches and to have been inherited by ancestors at deep nodes within the Poneria (Fig. 12). Future studies that aim for a more formal assessment may require refined character definitions, possibly based on precise quantifications,

Tab. 1: Taxa and specimens from Keller's Scanning Electron Microscopy atlas (Keller 2011) that were examined plus specimens from AntWeb (2022) that were included in the figures of this contribution.

Subfamily	Genus	Species	Authority	Identifier
Agroecomyrmecinae	*Agroecomyrmex*	*duisburgi*	(Mayr, 1868)	BMNHP18831
	Ankylomyrma	*coronacantha*	Bolton, 1973	CASENT0005904
				CASENT0902015
				MCZ:Ent:728292
	Tatuidris	*tatusia*	Brown & Kempf, 1968	ANTWEB1008593
				ANTWEB1008605
				CASENT0423526
				CASENT0178755
Amblyoponinae	*Adetomyrma*	*caputleae*	Yoshimura & Fisher, 2012	ANTWEB1008494
	Amblyopone	*australis*	Erichson, 1842	ANTWEB1008497
	Fulakora	*chilensis*	(Mayr, 1887)	ANTWEB1008496
		bath5	-	QMT152681
	Prionopelta	*amabilis*	Forel, 1909	ANTWEB1008581
	Prionopelta	*concenta*	(Brown, 1974)	ANTWEB1008513
	Stigmatomma	*pallipes*	(Haldeman, 1844)	ANTWEB1008501
Apomyrminae	*Apomyrma*	*stygia*	Brown & al., 1971	ANTWEB1008505
				CASENT0000077
Paraponerinae	*Paraponera*	*clavata*	(Fabricius, 1775)	ANTWEB1008572
				CASENT0006789
Ponerinae	*Platythyrea*	*punctata*	(F. Smith, 1858)	ANTWEB1008574
		turneri	Forel, 1895	ANTWEB1008575
	Anochetus	*emarginatus*	(Fabricius, 1804)	ANTWEB1008504
	Belonopelta	*deletrix*	Mann, 1922	ANTWEB1008507
	Bothroponera	*pachyderma*	(Emery, 1901)	ANTWEB1008567
	Brachyponera	*croceicornis*	(Emery, 1900)	ANTWEB1008564
	Centromyrmex	*brachycola*	(Roger, 1861)	ANTWEB1008505
	Cryptopone	*gilva*	(Roger, 1863)	ANTWEB1008514
	Dinoponera	*lucida*	Emery, 1901	ANTWEB1008517
	Dolioponera	*fustigera*	Brown, 1974	ANTWEB1008521
	Emeryopone	*buttelreepeni*	Forel, 1912	ANTWEB1008525
	Hagensia	*h. marleyi*	Arnold, 1926	ANTWEB1008566
	Harpegnathos	*saltator*	Jerdon, 1851	ANTWEB1008532
	Hypoponera	mx01	-	ANTWEB1008535
	Leptogenys	mx01	-	ANTWEB1008541
		np02	-	ANTWEB1008542
		podenzanai	(Emery, 1895)	ANTWEB1008543
	Loboponera	*vigilans*	Bolton & Brown, 2002	ANTWEB1008546
	Myopias	*maligna*	(F. Smith, 1861)	ANTWEB1008550
	Neoponera	*apicalis*	(Latreille, 1802)	ANTWEB1008561
		villosa	(Fabricius, 1804)	ANTWEB1008571
	Odontomachus	*bauri*	Emery, 1892	ANTWEB1008557
	Odontoponera	*transversa*	(F. Smith, 1857)	ANTWEB1008558
	Ophthalmopone	*berthoudi*	Forel, 1890	ANTWEB1008562
	Pachycondyla	*crassinoda*	(Latreille, 1802)	ANTWEB1008563

Subfamily	Genus	Species	Authority	Identifier
	Paltothyreus	*tarsatus*	(Fabricius, 1798)	ANTWEB1008570
	Phrynoponera	*pulchella*	(André, 1892)	ANTWEB1008573
	Platythyrea	*lamellosa*	(Roger, 1860)	CASENT0252018
	Plectroctena	*strigosa*	Emery, 1899	ANTWEB1008576
	Ponera	*alpha*	Taylor, 1967	ANTWEB1008578
	Psalidomyrmex	*procerus*	Emery, 1901	ANTWEB1008585
	Pseudoneoponera	*porcata*	(Emery, 1897)	ANTWEB1008568
	Pseudoponera	*stigma*	(Fabricius, 1804)	ANTWEB1008569
	Simopelta	*oculata*	Gotwald & Brown, 1967	ANTWEB1008588
		transversa	Mackay & Mackay, 2008	ANTWEB1008589
	Streblognathus	*peetersi*	Robertson, 2002	ANTWEB1008591
	Thaumatomyrmex	*fraxini*	D'Esquivel & Jahyny, 2017	ANTWEB1008597
	Wadeura	*guianensis*	Weber, 1939	ANTWEB1008565
Proceratiinae	*Discothyrea*	*oculata*	Emery, 1901	ANTWEB1008518
		testacea	Roger, 1863	ANTWEB1008519
	Proceratium	*creek*	De Andrade, 2003	CASENT0104439
		croceum	(Roger, 1860)	ANTWEB1008583
		pergandei	(Emery, 1895)	ANTWEB1008584
	Probolomyrmex	*guineensis*	Taylor, 1965	ANTWEB1008582
				CASENT0249253

considerations of character interdependencies, and expanded datasets including µ-CT-scans and additional SEM images. For heuristic purposes, we group the characters in Table 2 into possible apomorphies of certain clades and, for the head of *Tatuidris tatusia*, informal sets based on hypothesized functions of the included character states. Table 2 is not exhaustive given the limitation of image availability, yet we hope that it will be a useful foundation for future hypothesis testing and for future studies as a summary of similarities and differences across the taxa under consideration.

Results

Head capsule

A digital 3D model of the head to view from all angles is available on Sketchfab (https://skfb.ly/o8UAW). The head is roughly as large as the mesosoma in apparent total volume (Fig. 1). It appears orthognathous in dead specimens, that is, the mouthparts are oriented downwards, and the longitudinal cephalic axis is perpendicular to the longitudinal axis of the body. However, in living specimens, the head often has an oblique, subprognathous orientation, with an angle of the longitudinal axes of about 30° relative to the mesosoma (Fig. 1, see also live observations of a colony of *Tatuidris tatusia*; [https://www.youtube.com/watch?v=AkeNF9PW92s]; Jacquemin & al. 2014, 2018). The postocciput and the occipital foramen are set in a deep concavity on the ventral side of the head; they are almost perpendicular to the longitudinal axis of the head (Fig. 2C). The postocciput is hourglass-shaped in posterior view, with the upper portion much wider than the lower one and both separated by the postoccipital condyles (pocn, Fig. 2C). Proximad the ventromedian margin of the foramen, a secondary median evagination is present; this subforaminal process is hook-like and curved ventrad (sfp, Figs. 2C; 3B). The concave occipital region above the postocciput (occ, Fig. 2C) fits with the parabolic anterodorsal part of the pronotum, and the posterior declivity of the vertexal area (vt, Fig. 2C) fits against the complementary convex contact surface of the pronotum.

The strongly sclerotized head capsule is distinctly broader than long, rounded posterolaterally, and almost straight along the posterior margin, depending on the angle of view (Fig. 2A). The dorsal (frontal) surface forms an even and broad convexity (Brown & Kempf 1968: shield-shaped); its anterolateral margins consist of large, slightly raised frontal lobes (frl, Fig. 2A, B, D); they are weakly curved in lateral view and obliquely oriented in dorsal view, diverging posteriorly.

The shield-like frontal surface is almost indistinguishable from the clypeus (border roughly indicated as dotted line in Fig. 2A); only a slight swelling of the cuticle and the site of origin of the clypeobuccal and clypeopalatal muscles (0ci1, 0bu1) mark its location. The clypeus' anterolateral corners project anterad above the base of the mandible together with the frontal lobes (lcl, Fig. 2A). The anterior clypeal lamina (cll, Fig. 2D) forms the apparent anterior margin of the clypeus; it is broad and slightly sinuate,

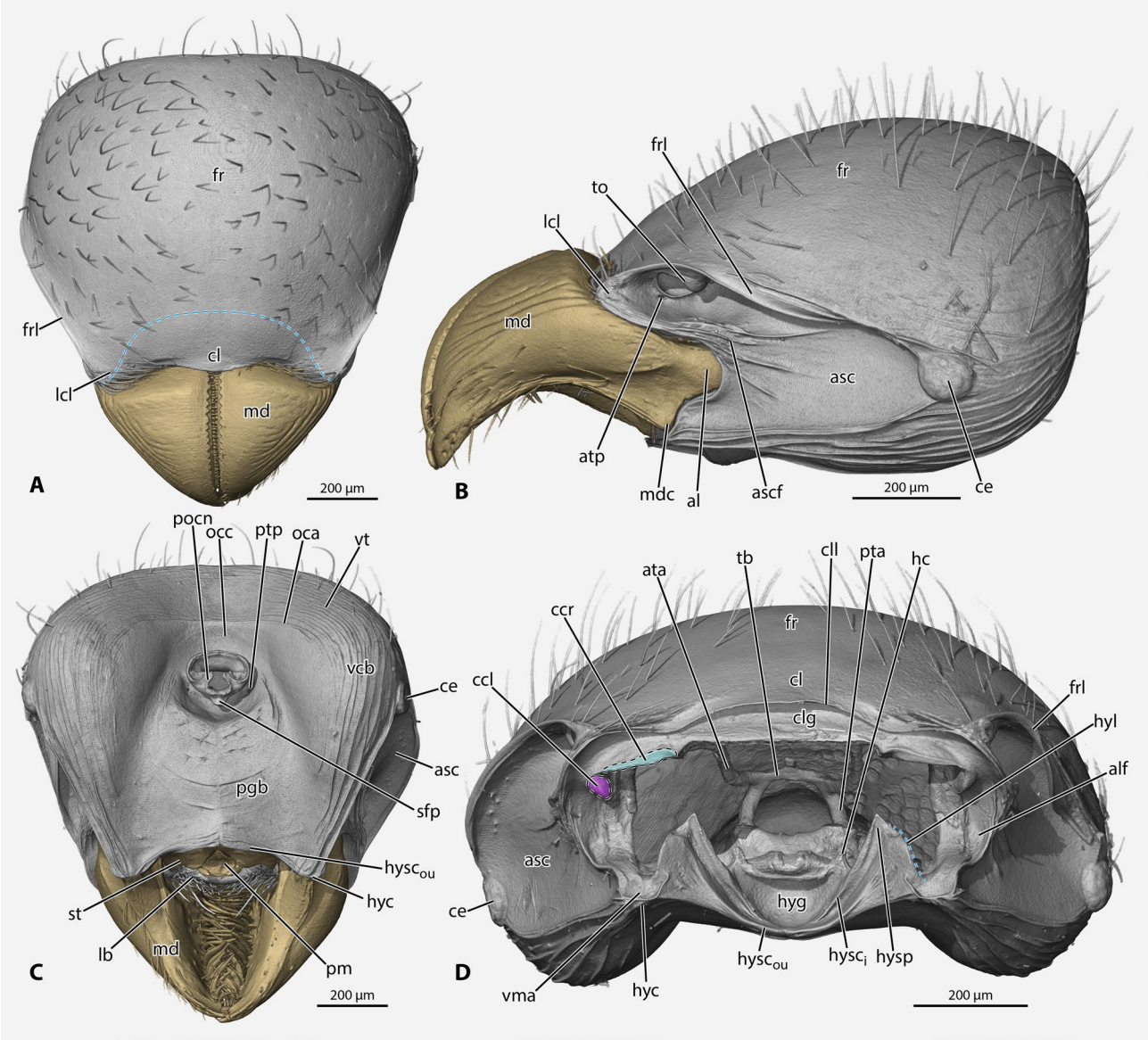

Fig. 2: Volume renderings of the head of *Tatuidris tatusia*, based on micro-computed tomography scan. **A:** Dorsal view. **B:** Lateral view. **C:** Ventral view. **D:** Frontal view of oral foramen showing articular surfaces of the mouthparts. **Abbreviations:** **al** – atala; **alf** – atalar fossa of the pleurostoma; **asc** –antennal scrobe; **ascf** – stabilizing ridges in the antennal scrobe; **ata** – anterior tentorial arm; **atp** – anterior tentorial pit; **ccl** – clypeal condylar lobe; **ccr** – clypeal condylar rail; **ce** – compound eye; **cl** – clypeus; **clg** – clypeal groove; **cll** – clypeal lamina; **fr** – frontal area; **frl** – frontal lobe; **hc** – hypostomal cardinal condyle; **hyc** – hypostomal corner; **hyg** – hypostomal groove; **hyl** – anterior lobe of the hypostomal process; **hysc$_i$** – inner hypostomal carina; **hysc$_{ou}$** – outer hypostomal carina; **hysp** – triangular hypostomal process; **lb** – labrum; **lcl** – lateral clypeal lobe (fused to frontal lobe); **md** – mandible; **mdc** – mandibular condyle; **oca** – occipital carina; **occ** – occipital area; **pgb** – postgenal bridge; **pm** – prementum; **pocn** – postoccipital condyle; **pta** – posterior tentorial arm; **ptp** – posterior tentorial pit; **sfp** – subforaminal process; **st** – stipes; **tb** – tentorial bridge; **to** – torulus; **vcb** – posterolateral ventral cephalic bulge; **vma** – ventral mandibular articulation fossa; **vt** – area of the vertex. ***Symbols*:** cyan dotted line – outline of the hypostomal process lobe in D and rough indication of the clypeal margin in A. **Color marking:** cyan – clypeal condylar rail; purple – clypeal condylar lobe.

Fig. 3: Volume renderings of the head, antenna, antennal articulation, and antennal musculature of *Tatuidris tatusia*, based on micro-computed tomography scan. **A:** Antennal musculature and tentorium, dorsal view on the left and ventral view on the right. **B:** Antennal musculature and inner skeleton in sagittal view. **C:** Lateral view of head with antenna in antennal scrobe.

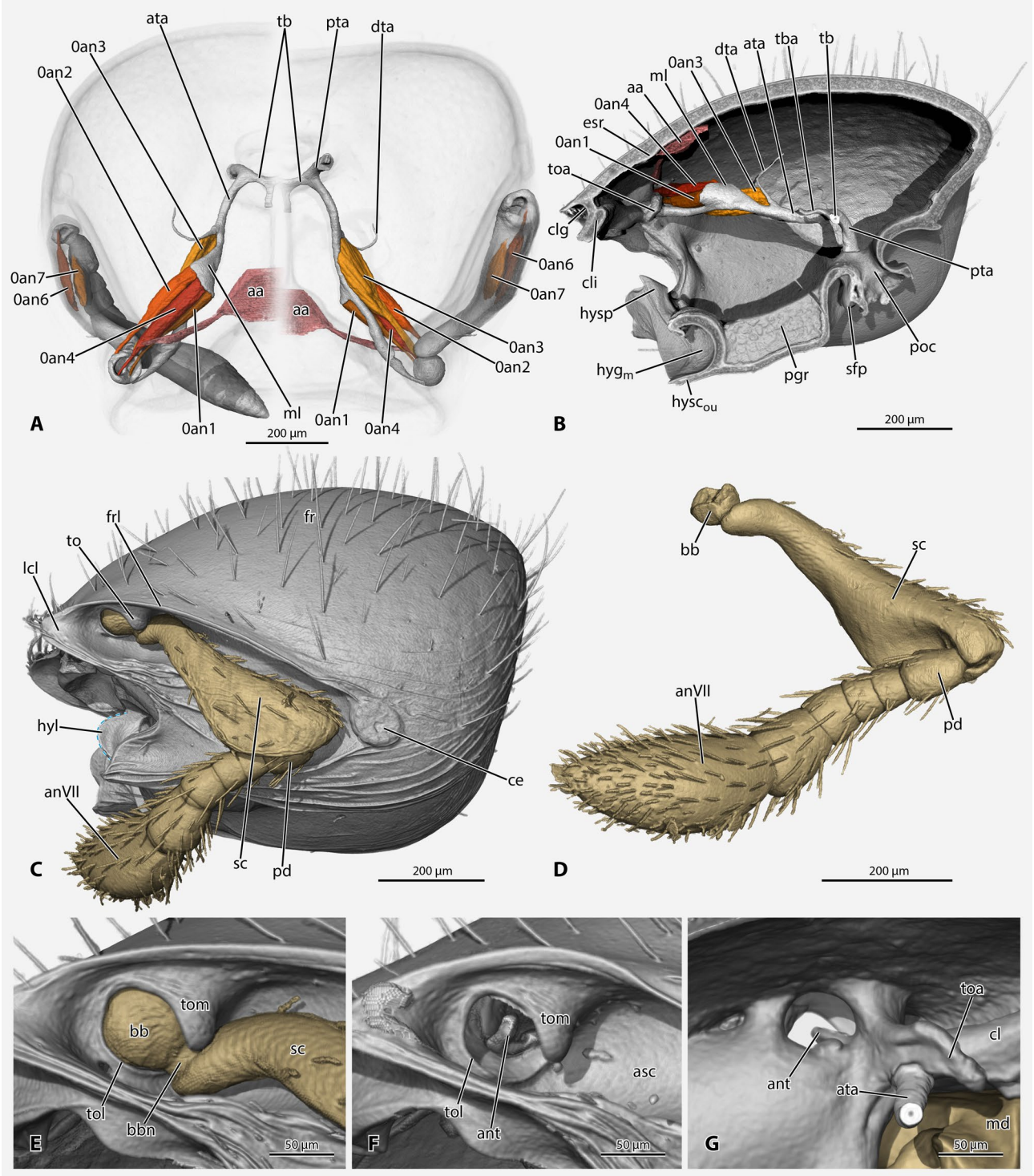

D: Medial view of antenna. **E:** Antennal articulation in ventrolateral view. **F:** As in C but with antenna removed. **G:** Antennal articulation in internal posterior view. **Abbreviations: 0an1** – M. tentorioscapalis anterior; **0an2** – M. tentorioscapalis posterior; **0an3** – M. tentorioscapalis lateralis; **0an4** – M. tentorioscapalis medialis; **0an6** – M. scapopedicellaris lateralis; **0an7** – M. scapopedicellaris medialis; **aa** – antennal ampulla; **anVII** – antennomere seven / apical antennomere; **ant** – antennifer; **asc** – antennal scrobe; **ata** – anterior tentorial arm; **bb** – bulbus; **bbn** – bulbus neck; **cl** – clypeus; **clg** – clypeal groove; **cli** – clypeal inflection; **ce** – compound eye; **dta** – dorsal tentorial arm; **esr** – vestige of the epistomal ridge; **fr** – frontal area; **frl** – frontal lobe; **hyg_m** – median hypostomal groove; **hyl** – anterior lobe of the hypostomal process; **$hysc_{ou}$** – outer hypostomal carina; **hysp** – triangular hypostomal process; **lcl** – lateral clypeal lobe (fused to frontal lobe); **md** – mandible; **ml** – medial lamella; **pd** – pedicel; **pgr** – postgenal ridge; **poc** – postocciput; **pta** – posterior tentorial arm; **sc** – scapus; **sfp** – subforaminal process; **tb** – tentorial bridge; **tba** – anteriomedial process of the tentorial bridge; **to** – torulus; **toa** –torular apodeme; **tol** – lateral torular arch / torular lobe; **tom** – median torular arch. **Symbols:** cyan dotted line – outline of the hypostomal process.

protruding medially; its marginal area presents a fine, transverse imbricate surface pattern; on each lateral side of the lamina groups of conspicuous mesally directed, curved setae are present. The inflected portion of the clypeus forms a deeply concave and dorsoventrally broad groove / sulcus (clg, Fig. 2D); it is continuous across the dorsal margin of the oral foramen and curves laterad around the mandibular base; the groove is dorsally and laterally walled off by the anterior clypeal lamella; it bears two pairs of thin setae. Laterally, the clypeus is delimited by the anterior tentorial pit, which is situated inside the antennal scrobe close to the antennal socket (atp, Fig. 2B), and by a short internal ridge between the antennal socket and the dorsal mandibular articulation. The clypeal surfaces articulating with the mandibles are L-shaped and wide along the lateromedial axis; the short clypeal condylar lobes (ccl, Fig. 2D) are longitudinal to the long axis of the head, while the long clypeal condylar rails (ccr, Fig. 2D) are transversely oriented. A supraclypeal area or a frontal line are at most very indistinctly indicated by a flat cuticular depression (Fig. 2A).

The widely separated antennal foramina are not visible in dorsal (frontal) view; their position is only indicated by low, dome-like bulges of the frontal lobes. The torular sclerite itself is situated within a deep antennal scrobe and oriented ventrad (to, Fig. 2B). The antennal scrobe is large, triangular, and deep, covering a major portion of the lateral head surface (asc, Fig. 2B); it reaches the posterior third of the head capsule, where the small, roughly circular and convex compound eyes are inserted (diameter ca. 80 µm). The scrobe is delimited dorsally by the expanded frontal lobe (frl, Fig. 2A, B, D); a narrower but distinct longitudinal ridge forms its ventral border. The scrobe is medially divided into a dorsal and a ventral portion by the lateral edge of the anteriorly produced clypeus; some longitudinal costae / ridges stretch posteriorly into the antennal scrobe from this point (ascf, Fig. 2B). Internally, the scrobal surface does not bear muscular attachments.

On the ventral side of the head, the posterolateral regions form pronounced bulges (vcb, Fig. 2C); these bulges extend well below the ventromedian cephalic surface and narrow anteriorly towards the ventral (primary) mandibular articulations; curved, longitudinal ridges / costae are present on their surface. Internally, the bulges are filled out with fibers of the mandible adductor / closer muscle (0md1). Between the bulges, the ventral surface of the head is roughly triangular (Fig. 2C), with a boxy postgenal region delimited laterally by wide grooves that narrow as they enter the occipital concavity. The postgenal region (pgb, Fig. 2C) is divided into anterior and posterior portions by an arcuate, discontinuous carina that posteriorly ends laterad the posterior tentorial pits; this carina may be the ventral rim of the occipital carina. The posterior portion of the postgenal region bears a few short setae. The postgenal bridge and the internal postgenal ridge are short relative to the head length (pgb length / cephalic length = 0.415, n = 1), resulting in the subprognathous / oblique head orientation.

Seen from below, the hypostomal margin appears weakly concave ($hysc_{ou}$, Fig. 2C), eclipsing the anterior clypeal margin in a low, oblique posteroventral view; the depth of this margin from the anterolateral hypostomal corners (hyc, Fig. 2C) is about 1 / 5 of its lateromedial width (vs. ~ 1 / 2 in other ants). Due to the shallowness of the hypostoma, the maxillolabial complex is held in an almost vertical orientation in its retracted position. It is noteworthy that the curvature of the hypostomal margin is similar to that of the posterior clypeal margin (compare Fig. 2A, C). The outer hypostomal carina ($hysc_{ou}$, Fig. 2C, D) bears transverse cuticular ridges externally (Fig. 2C). Ventrally, the outer carina delimits the deep hypostomal groove (hyg, Fig. 2D); laterally, it reaches the flat hypostomal corners (hyc, Fig. 2C, D). The inner hypostomal carina ($hysc_{i}$, Fig. 2D) ends laterally in the tips of the triangular hypostomal processes (hysp, Fig. 2D) and reaches the outer hypostomal carina medially. The anterolateral margins of the triangular processes bear broad, anteriorly directed, rounded lobes (hyl, Fig. 2D).

The cuticle of the head is dark brown and shiny. A regular vestiture of setae of about 70 µm length is present; the average distance between setae is about 50 µm.

Endoskeleton

The anterior tentorial arms are long and curved in a complicated manner (ata, Fig. 3A, B); they are slightly sinuous, in both sagittal as well as dorsal or ventral view; in dorsal or ventral view their posterior halves are roughly parallel while their anterior halves are strongly diverging. The posterior tentorial arms are dorsally directed and sharply curved anteriad (ca. 90°) at the level of the tentorial bridge (pta, Fig. 3A, B). This configuration results in an almost horizontal orientation of the anterior tentorial arms relative to the longitudinal axis of the head capsule (Fig. 3B). The medial tentorial lamella (ml, Fig. 3A, B) forms a short lobe that is twisted upwards, resulting in almost horizontal orientation of the extrinsic antennal muscles (0an1 - 4, Fig. 4A, B). The lateral lamella is absent. The dorsal tentorial arm is long and consists of a relatively thick base and a thin, thread-like extension; the latter structure is directed backward on one side and forward on the other, indicating that it is relatively flexible (dta, Fig. 3A, B). The tentorial bridge is very short and thinner than the posterior arms (tb, Fig. 3A, B); a rather long and thick anteromedian process is continuous with the tendon of 0bu5 / 6 (tba, Fig. 3A, B). The epistomal ridge is vestigial, and only a slight thickening of the cuticle can be observed in its place (esr, Fig. 3B). The postgenal ridge extends over the entire width of the short, box-like postgenal bridge (pgr, Fig. 3B). The torular apodemes are formed by dorsoventrally flattened, rod-like processes, extending mesad from the antennal socket and slightly curved anteriad (toa, Fig. 3B, G).

The antennae and their articulations

The antennal foramen and antennal base are covered by the large frontal lobe; the ventrally facing antennal

socket apparatus is placed on the ventral surface of this projection (Fig. 3C). Due to this rotation of the antennal socket, the medial arch of the torulus (tom, Fig. 3E) is positioned laterad the lateral arch (tol, Fig. 3E). The torular lobe of the medial arch is well-developed, roughly triangular, but apically rounded; it is located on the posterior half of the torulus (tom, Fig. 3E, F). The antennal acetabulum is a large concave area on the dorsal, anterior, and ventral torular surfaces; the massive antennifer is located at the anterior margin of the foramen and is almost transversely oriented (ant, Fig. 3F, G). It articulates with the bulbus (bb, Fig. 3C - E), which is hemispherical and deeply countersunk into the acetabulum. The short bulbus neck is almost cylindrical but slightly widens distally (bbn, Fig. 3E); it is attached to the posterior side of the bulbus and separated from the main shaft of the scapus by a constriction. The seven-merous (= "segmented") geniculate antenna fits almost completely into the antennal scrobe except for the large apical flagellomere, with the scape and flagellum fitting into the dorsal and ventral portions of the scrobe, respectively (Fig. 3C). When the antenna is pulled back, the movement is restricted by the large torular lobe (Fig. 3E), confining it to a resting position in the antennal scrobe. The scapus (sc, Fig. 3C - E) is slightly longer than the pedicellus (pd, Fig. 3C, D) and flagellomeres 1 - 4 combined; it is bent at about 45° close to the bulbus neck, curving anteriad in its proximal half; its anterior margin forms a broad distal lobe, resulting in a clavate appearance of the entire antennomere; this distal lobe is broadly concave and receives the pedicellus when the flagellum is flexed towards the scapus body; the anterior distal margin of the scapus is deeply notched to create space for pedicellus movements (Fig. 3D). The pedicellus is about 1 / 5 as long as the scapus; its base is narrowed and slightly curved anteriad. Flagellomeres 1 - 4 widen distally, appearing cup-shaped; their size increases towards the antennal apex. The spindle-shaped apical antennomere is enlarged, about 2 / 3 as long as the scapus (anVII, Fig. 3C, D); the density of setae is slightly increased apically; a field of sensilla placodea, each with a distinct perforation, is present apically (Keller 2011).

Musculature (Fig. 3A, B): Due to the switch in the orientation of the antennal socket, the bulbus is also shifted. Its medial margin is dorsal and more lateral than the ventrally shifted lateral margin, and the bulbus is rotated so that the anterior muscle is inserted medially, the posterior one laterally, the lateral one anteriorly, and the medial one anteriorly. Nevertheless, relative positions of origin on the tentorium are retained, so that homologization with other ants is possible. **Musculus tentorioscapalis anterior (0an1):** origin (= **O):** anterior / dorsal surface of the medial tentorial lamella, on its anterior corner; insertion (= **I):** on a tendon originating medially on the bulbus. **M. tentorioscapalis posterior (0an2): O:** posteriorly on the anterior / dorsal surface of the medial tentorial lamella, posteriad 0an4; **I:** on a tendon originating laterally on the bulbus. **M. tentorioscapalis lateralis (0an3)**: largest of the four muscles; **O:** laterally on anterior tentorial arm; laterad / ventrad the other three muscles, partly on the dorsal tentorial arm; **I:** on a tendon originating posteriorly on the bulbus. **M. tentorioscapalis medialis (0an4): O:** anterior / dorsal on medial tentorial lamella, in between 0an1 and 0an2; **I:** on a tendon originating anteriorly on the bulbus. **M. scapopedicellaris lateralis (0an6): O:** dorsally on the distal half of the scapus; **I:** on a short tendon originating from the dorsal base of the pedicellus. **M. scapopedicellaris medialis (0an7): O:** ventrally on the distal half of the scapus; **I:** on a short tendon originating from the ventral base of the pedicellus.

The mandibles and their articulations

The massive, shovel-shaped mandibles are triangular in dorsal view, with the proximal stem and basal margin of the blade set at about a 90° angle (Fig. 4A, C). In ventral view, the thick mandibular stem appears swollen, with a lateral bulge towards the level of the mandibular blade (Fig. 4D); the bulge continues onto the mandibular blade dorsally and is visible in medial view near the basal margin (mdd, Fig. 4A, B, D). Posteriad the bulge, the blade tapers towards the slightly concave basal margin (bm, Fig. 4C, D), creating a broad, sloping surface (sms, Fig. 4C, E). The basal margin fits into the clypeal groove (bmc, Fig. 4B) but only in the medial clypeal region at the level of the labral articulation; it is subtended by a row of setae on the inner side of the mandible (Fig. 4D). A narrow ridge from the mandibular condyle to the apical tooth, the condylar carina (cdc, Fig. 4D), forms the ventral mandibular margin. At full closure, the medial / masticatory margins of the mandibles are aligned along their length; only the short and blunt triangular apical (ai, Fig. 4D, E) and subapical incisors (sai, Fig. 4C, D) overlap. The blade is roughly triangular in cross-section, with massive ventral and lateral portions and a thin medial portion towards the masticatory margin. In medial view, the blade is distally bent downwards and appears cup- or bowl-shaped, with a slightly concave internal surface (Fig. 4B, E).

The tool edge of the mandible comprises a complex of structures, including the masticatory margin (mm, Fig. 4C), the fimbrial line carina (flc, Fig. 4C, E), two specified sets of chaetae ("traction setae") (mdb, Fig. 4B, D, E), and thin sensory hairs (setae): The masticatory margin consists of a crenulate bead forming a row of denticles (cb, Fig. 4C, E); this bead is closely subtended ventrally by the fimbrial line carina (flc, Fig. 4C, E), which is a straight, sharp rim that continues proximally along the basal margin. Closely subtending the fimbrial line carina ventrally is the first specified line of chaetae, which is a single-file row of very short and bristle-like chaetae that are even in length and, with the masticatory margin, sandwich the fimbrial carina between sharp points. This chaetal line is ventrally subtended by the second chaetal set; this dense patch of robust and acuminate chaetae (mdb, Fig. 4A, B, D, E) is curved toward the masticatory margin and gradually lengthens toward the lateral mandibular edge; the longest chaetae are very slightly sinuate; all chaetae are set in deep

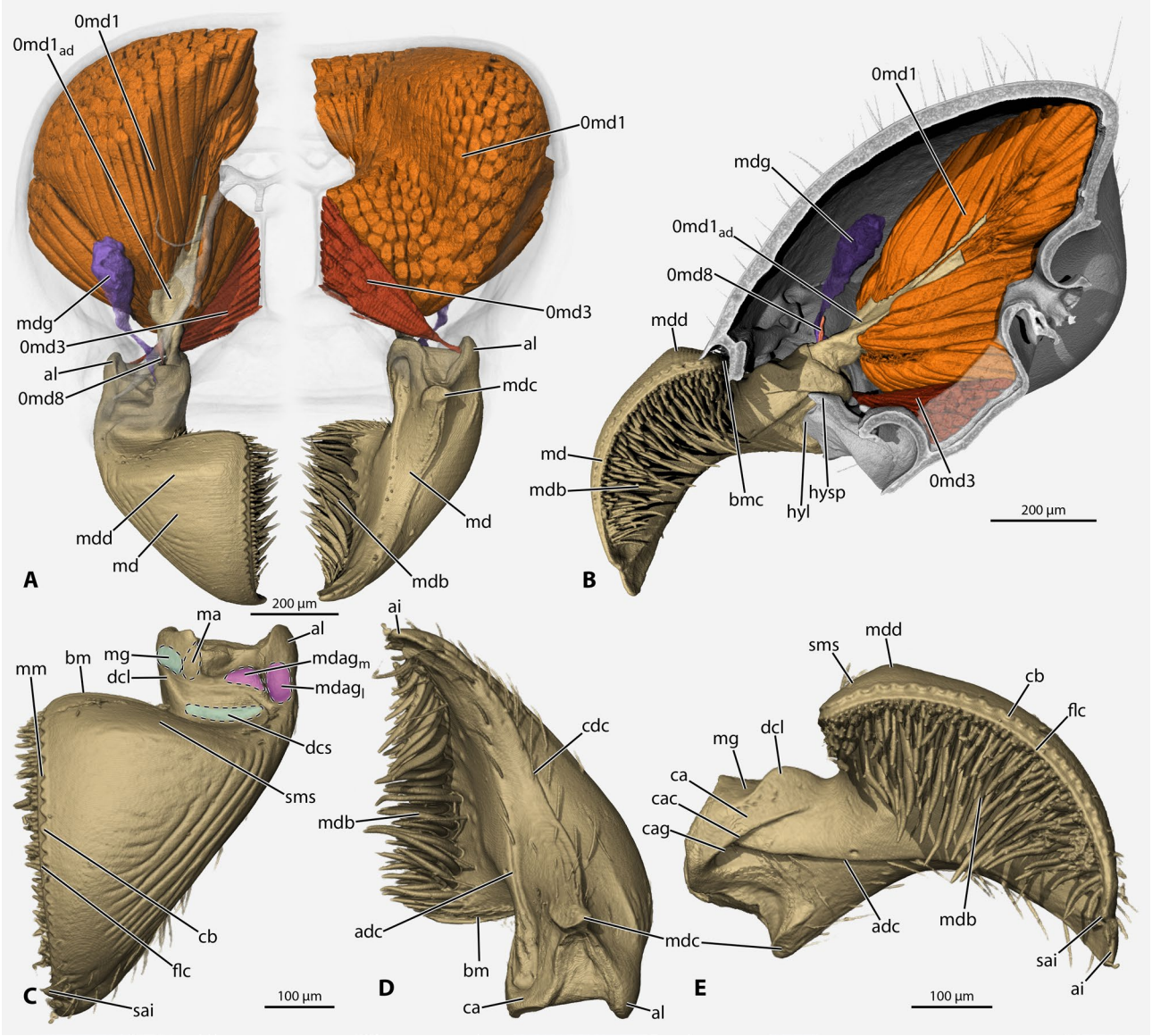

Fig. 4: Volume renderings of the mandible, mandibular musculature, and mandibular gland of *Tatuidris tatusia*, based on micro-computed tomography scan. **A, B:** Mandibular muscles and gland. **A:** Dorsal view left, ventral view right. **B:** Sagittal view. **C - E:** Details of the mandible. **C:** Dorsal view. **D:** Ventral view. **E:** Medial view. **Abbreviations: 0md1** – M. craniomandibularis internus; **$0md1_{ab}$** – M. craniomandibularis internus apodeme; **0md3** – M. craniomandibularis externus; **0md8** – M. tentoriomandibularis; **ai** – apical incisor; **adc** – adductor carina; **al** – atala; **bm** – basal margin; **bmc** – basal margin resting in clypeal groove; **ca** – canthellus; **cac** – canthellar carina; **cag** – canthellar groove; **cb** – crenulate bead; **cdc** – condylar carina; **dcl** – dorsal canthellar lobe; **dcs** – distal mandibular contact surface; **flc** – fimbrial line carina; **hyl** – anterior lobe of the hypostomal process; **hysp** – triangular hypostomal process; **ma** – mandalus; **md** – mandible; **$mdag_l$** – lateral mandibular acetabular groove; **$mdag_m$** – medial mandibular acetabular groove; **mdb** – mandibular chaetal brush; **mdc** – mandibular condyle; **mdd** – mandibular dorsal bulge; **mdg** – mandibular gland; fimbrial carina; **mg** – medial mandibular groove; **mm** – masticatory margin; **sai** – subapical incisor; **sms** – sloping surface of proximal mandibular blade. **Color marking:** cyan – contact surfaces of clypeal condylar rail; purple – contact surfaces of clypeal condylar lobe.

pores (Fig. 5B) and have a surface pattern of oblique riffles. Sensory setae are loosely arranged along the smooth region of the concave inner mandibular surface. The acetabular carina (adc, Fig. 4E) is a well-developed, oblique ridge accompanied by an oblique row of setae, separating the fimbrial / brush area from the convex ventral mandibular surface; distally, it reaches the subapical tooth.

The ventral (primary) mandibular condyle (mdc, Fig. 4A, D, E), a short and narrow ventral projection on the central area of the mandibular stem, is slightly curved laterad; the corresponding articulatory fossa (vma, Fig. 2D) is placed at the very anterior edge of the ventral head capsule on the hypostomal corner (hyc, Fig. 2C, D); the fossa is slightly wider than long; it is stabilized by the

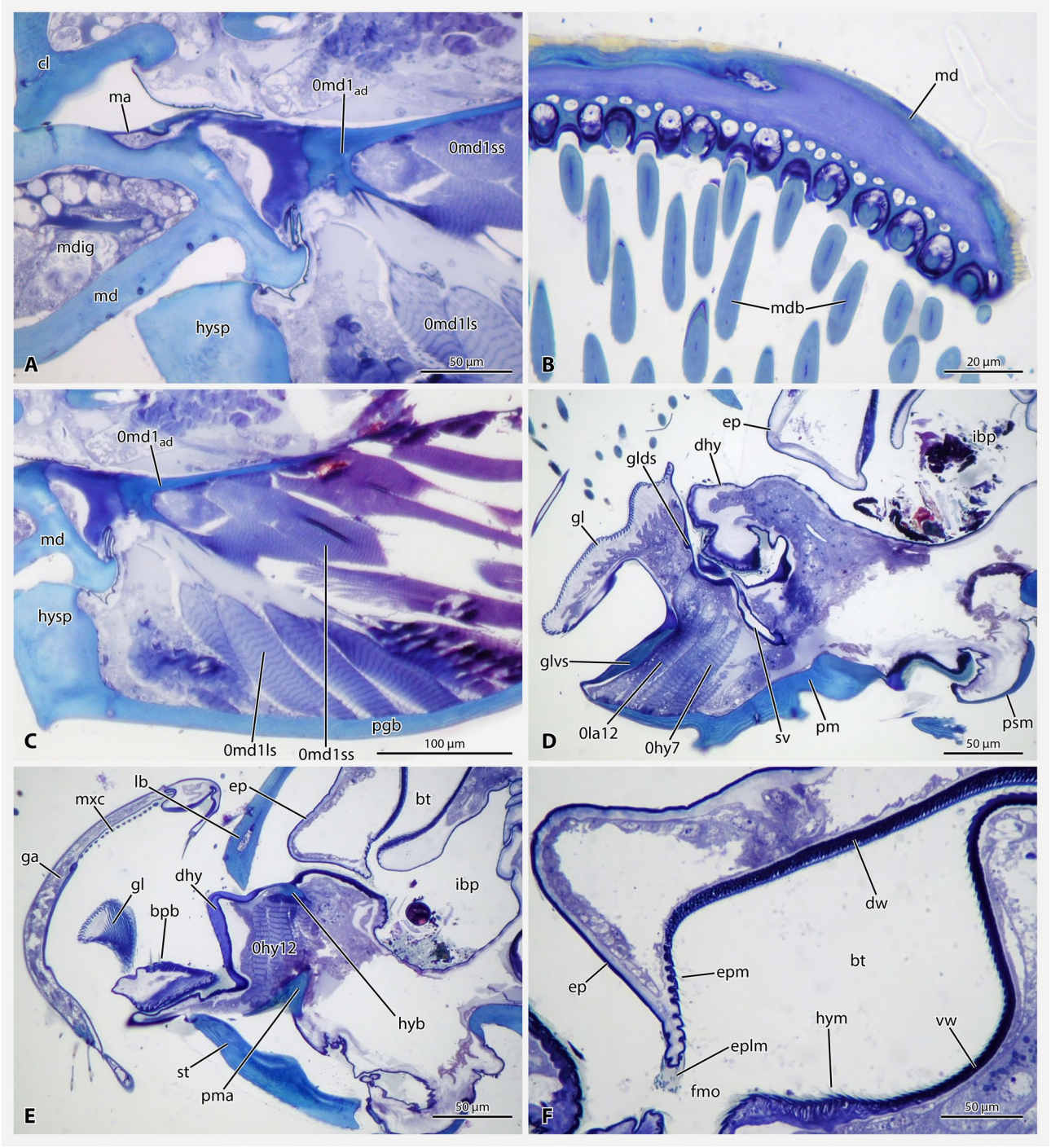

Fig. 5: Longitudinal histological sections through the head of *Tatuidris tatusia*. **A:** Base of the mandible, showing part of the mandalus and the inner mandibular gland. **B:** Tip of the mandible, showing the chaetal brush in its deep pores. **C:** Lateral head region, section through the center of the 0md1 muscle and its apodeme, showing different fiber types. **D:** Roughly sagittal section showing labium, distal hypopharynx, and infrabuccal pouch. **E:** Section slightly laterad of B, additionally showing galea and stipes. **F:** Roughly sagittal sections showing buccal tube. **Abbreviations: 0hy7** – M. praementosalivarialis; **0hy12** – M. hypopharyngosalivarialis; **0la12** – M. praementoglossalis; **0md1ad** – M. craniomandibularis internus apodeme; **0md1ls** – M. craniomandibularis internus, long sarcomere fiber; **0md1ss** – M. craniomandibularis internus, short sarcomere fiber; **bpb** – basiparaglossal brush; **bt** – buccal tube; **cl** – clypeus; **dhy** – distal hypopharynx; **dw** – dorsal (epipharyngeal) prepharyngeal wall; **ep** – epipharynx; **epm** – epipharyngeal microtrichia; **eplm** – epipharyngeal lip microtrichia; **fmo** – functional mouth opening; **ga** – galea; **gl** – glossa; **glds** – glossa dorsal sclerite; **glvs** – glossa ventral sclerite; **hyb** – hypopharyngeal rod; **hym** – hypopharyngeal microtrichia; **hysp** – triangular hypostomal process; **ibp** – infrabuccal pouch; **lb** – labrum; **ma** – mandalus; **md** – mandible; **mdb** – mandibular chaetae brush; **mdig** – inner mandibular gland; **mxc** – maxillary comb; **pgb** – postgenal bridge; **pm** – prementum; **pma** – premental arm; **psm** – postmentum; **st** – stipes; **sv** – salivarium; **vw** – ventral (hypopharyngeal) prepharyngeal wall.

longitudinal costae on the ventrolateral surface of the head capsule, which converge in this point. The evenly rounded atala (al, Fig. 4A, D) is a large lateral projection of the mandibular stem; it reaches about half the vertical extension of the mandibular base and is inserted in a large acetabulum laterad the oral foramen (alf, Fig. 2D). The dorsal (secondary) mandibular articulation consists of an L-shaped clypeal condyle, described in the head capsule section above (ccr, cdl Fig. 2D), and the corresponding, complicated acetabular surfaces of the mandibular stem. In the resting position, the condylar lobe is received by the small lateral mandibular acetabular groove ($mdag_l$, Fig. 4C); the lateral acetabular groove is separated from a medial acetabular groove by a short ridge ($mdag_m$, Fig. 4C). When the mandible opens, the condylar lobe traverses the ridge and locks into the medial groove, as shown by our 3D-printed model manipulations (see section "Possible mandibular motions" below). Anteromediad of the acetabular grooves, a smooth, broad area forms the distal contact surface of the mandibular stem (dcs, Fig. 4C); this smooth region serves as a secondary acetabular region receiving the condylar rail. Mesally, the surface is bordered by a lobe of the canthellus (dcl, Fig. 4C) and a slanted, slightly concave area on the medial side of the mandibular stem, which forms the medial mandibular groove (mg, Fig. 4C). According to our mechanical tests, the condylar rail slides along the canthellar lobe and the medial groove as the mandible opens (see section "Possible mandibular motions"). The canthellus itself is an oblique medial thickening on the dorsal half of the mandibular base (ca, Fig. 4E); it is capped ventrally by a carina (cac, Fig. 4E) that overhangs a groove (cag, Fig. 4E) into which the hypostomal process inserts when the mandible is flexed (closing) (Fig. 4B). The mandalus (ma, Figs. 4C, 5A) is represented by a small, paddle-shaped area dorsally on the mandibular stem, located laterad the medial groove (dorsal acetabular surface).

Musculature (Figs. 4A, B; 5A): Musculus craniomandibularis internus (0md1): by far the largest muscle in the head, filling most of the lateral head capsule; **O:** all of the posterior, most of the ventral, part of the dorsal, and some of the lateral head capsule except for the area of the antennal scrobe; **I:** Most fibers insert directly on the massive, sheet-like adductor apodeme. Only the outermost fibers of the muscle insert on the apodeme through rather short, thin cuticular fibrillae. Additionally, the fibers of a bundle originating dorsad of the occipital foramen insert with thin cuticular fibers on an accessory branch of the main apodeme. While sarcomeres are not visible in the µ-CT data of the central, directly attaching fibers, they are clearly recognizable in the thread attached fibers and also some of the directly attaching fibers at the edges of the apodeme, indicating that these may have longer sarcomeres. A few muscle fibers are visible on our histological sections, confirming that the fibers without visible sarcomeres in µ-CT data have shorter sarcomeres (Fig. 5A). **M. craniomandibularis externus (0md3): O:** mostly on the postgenal ridge and partly on the ventral head capsule; **I:** with a short tendon on the ventral side of the large atala. **M. tentoriomandibularis medialis inferior (0md8):** minute muscle of only two thin fibers; **O:** ventrally on the anterior tentorial arm; **I:** dorsomesal inner margin of the mandible.

Maxillae

The maxillae are closely connected to the labium by a conjunctiva, thus forming the maxillolabial complex. The cardines articulate with thin hypostomal cardinal condyles (hc, Fig. 2D). The external stipital sclerite (st, Fig. 6C) is elongate, more than twice as long as wide; its external surface bears a longitudinal furrow that is deepest proximally; a deep oblique groove runs across the sclerite distomedially (msg, Fig. 6C) and receives the distal labral margin in resting position. Apicolaterally, the stipital sclerite is produced as an acutely triangular process with a narrow, rounded tip, a concave medial side, and a convex lateral side (stp, Fig. 6C); in resting position, this process presses against the proximolateral labral process, locking the labrum in place (lbrp, Fig. 7B). The lateral margin of the stipes inserts into the concave anterior surface of the triangular hypostomal process (Fig. 7A). Most of the stipital surface bears a scale-like pattern of cuticular ridges; these ridges are arranged transversely on the proximal region and longitudinally on the lateral region; the concavity in the stipital center is mostly smooth except for some oblique rugae. The base of the inner stipital wall forms a short inner stipital sclerite; it continues onto the basal lacinial sclerite. The stipitopremental conjunctival thickening (spc, Fig. 7B) is large, curved, and connects the internal stipital sclerite with the premental arms and the hypopharynx at the lateral edge of the infrabuccal pouch (ibp, Fig. 7B). The large galeolacinial complexes are bent across the labium and distal hypopharynx. The apex of the galea (ga, Fig. 6C - E) is roughly triangular with rounded edges, the remaining galea roughly rectangular. It bears the maxillary comb of densely set, thick setae on its inner surface (mxc, Figs. 5C; 6E). The lacinia (lc, Fig. 6D, E) is roughly triangular and its margin is set with thick, spine-like hairs forming the lacinial comb (lcc, Fig. 6D). The maxillary palp is reduced and lacks musculature. The presence of a potential remnant of the palp could not be verified here; Bolton (2003) recorded one maxillary palpomere for *Tatuidris tatusia*.

Musculature (Fig. 6A, B): Musculus craniocardinalis externus (0mx1): O: posterior postgenal bridge below occipital foramen; **I:** lateral proximal base of the cardo. **M. tentoriostipitalis anterior (0mx4): O:** on the anterior tentorial arm close to the anterior tentorial pit; **I:** on a short process of the stipes in the region of the cardinostipital hinge. **M. tentoriostipitalis posterior (0mx5):** two bundles; **O:** anterior bundle on the anterior tentorial arm on the level of the medial lamella and partly on this lamella, posterior bundle posteriad the dorsal tentorial arm on the anterior arm; **I:** uniting tendons of the two bundles insert on the inner stipital sclerite. **M. stipitolacinialis (0mx6): O:** in the distolateral region

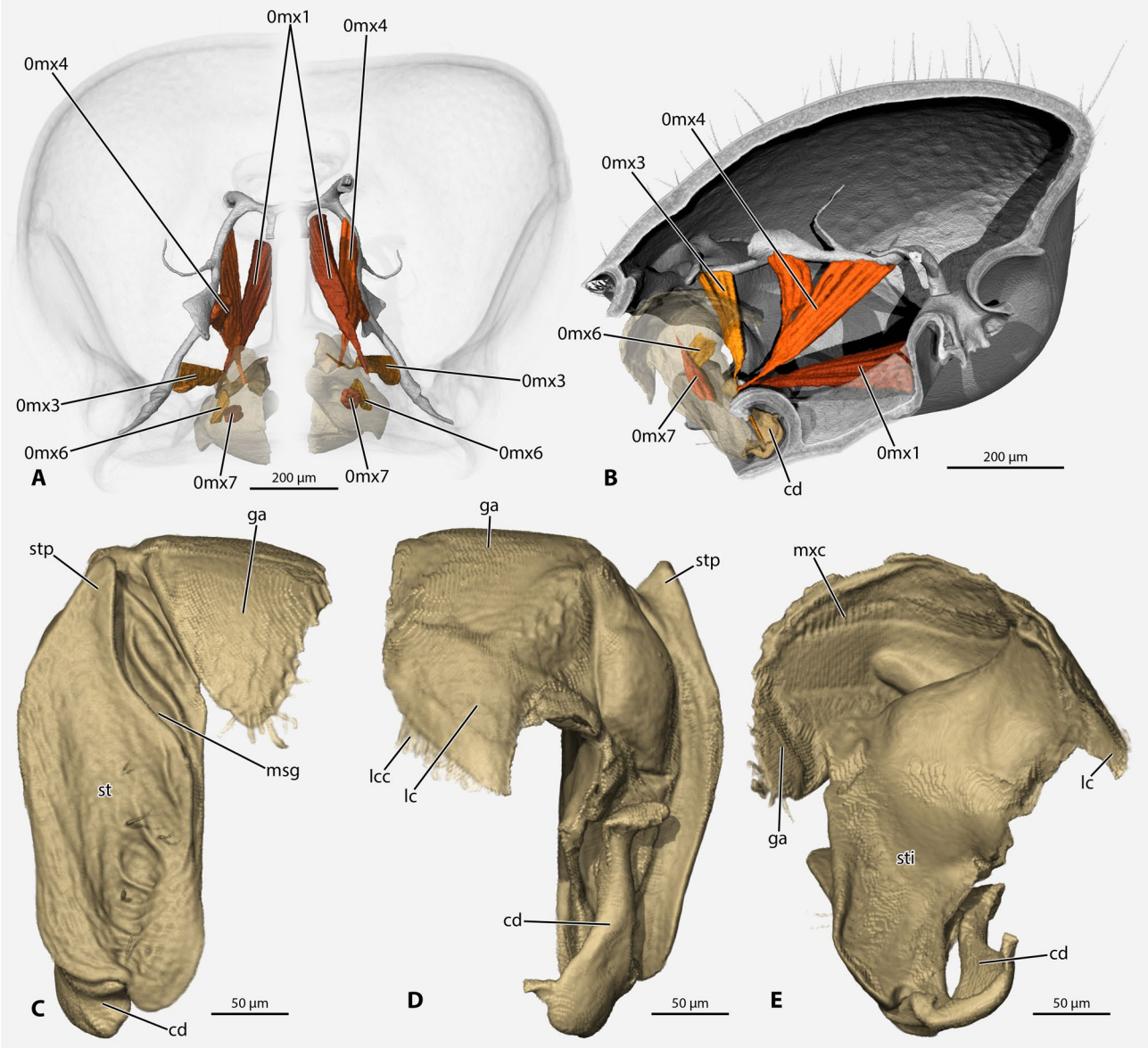

Fig. 6: Volume renderings of the maxilla and maxillary musculature of *Tatuidris tatusia*, based on micro-computed tomography scan. **A, B:** Maxillary muscles. **A:** Dorsal view left, ventral view right. **B:** Sagittal view. **C - E:** Details of the maxilla. **C:** Frontal view. **D:** Posterior view. **E:** Medial view. **Abbreviations: 0mx1** – M. craniocardinalis externus; **0mx3** – M. tentoriocardinalis; **0mx4** – M. tentoriostipitalis anterior; **0mx6** – M. stipitolacinialis; **0mx7** – M. stipitogalealis; **cd** – cardo; **ga** – galea; **lc** – lacinia; **lcc** – lacinial comb; **msg** – medial stipital groove; **mxc** – maxillary comb; **st** – outer stipital sclerite; **sti** – inner stipital wall; **stp** – stipital process.

of the external stipital sclerite; **I:** base of the lacinia. **M. stipitogalealis (0mx7): O:** centrally on the external stipital sclerite; **I:** with a short, thin tendon at the base of the galea. **M. stipitopalpalis externus (0mx8):** absent. **Intrinsic muscles of the maxillary palp**: absent.

Labium and distal hypopharynx

The short and narrow postmentum (psm, Figs. 5B; 8C, D) is located between the cardines and connected to them by the articulatory conjunctiva; together with the cardines, it is inserted in the deep hypostomal groove. In resting position, the base of the maxillolabial complex formed by the cardines and postmentum is covered by the medial edges of the external stipital sclerites and thus not visible externally (Fig. 7A). The ventral premental face consists of two roughly equally-sized parts, delimited by a deep transverse furrow (pmf, Fig. 8B - D); this furrow receives the distal margin of the labrum at full labral closure (Figs. 7A; 8B). The proximal portion (pmvp, Fig. 8C, D) has the shape of a circular sector, is irregularly wrinkled, and is the only part of the prementum visible externally in resting position; the distal premental portion (pmvd, Fig. 8C, D) is semi-elliptic and completely smooth. The thin and clavate two-segmented labial palps (plb, Fig. 8C - E) are inserted apicolaterally at the edge of the distal premental portion; both palpomeres are flattened basally and widen

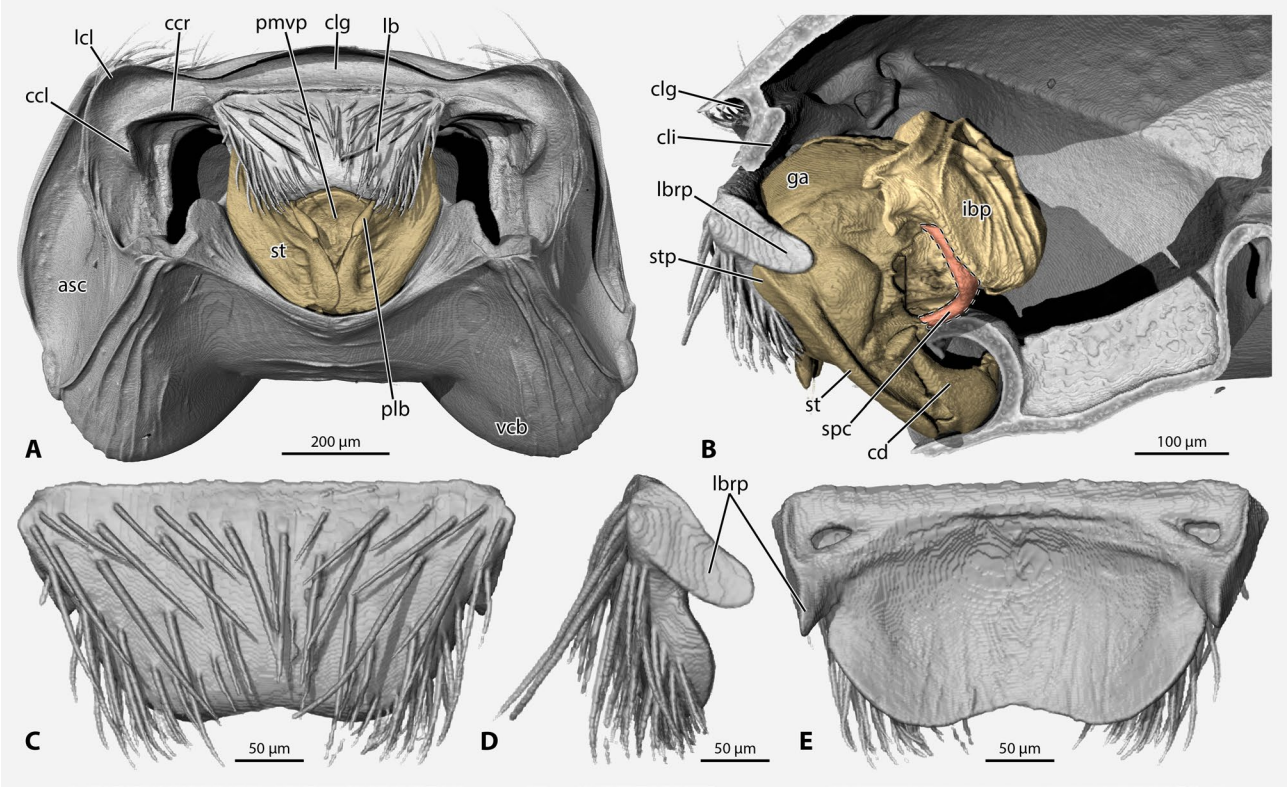

Fig. 7: Volume renderings of the head, labrum, and maxillolabial complex of *Tatuidris tatusia*, based on micro-computed tomography scan. **A:** Frontoventral view of maxillolabial-labral locking. **B:** Lateral view of maxillolabial-labral locking. **C - E:** Labrum. **C:** Outer surface. **D:** Lateral view. **E:** Inner surface. **Abbreviations: asc** – antennal scrobe; **ccl** – clypeal condylar lobe; **ccr** – clypeal condylar rail; **cd** – cardo; **clg** – clypeal groove; **cli** – clypeal inflection; **ga** – galea; **ibp** – infrabuccal pouch; **lb** – labrum; **lbrp** – proximolateral labral process; **lcl** – lateral clypeal lobe (fused to frontal lobe); **plb** – labial palp; **pmvp** – ventral premental surface; **spc** – stipito-premental conjunctival thickening; **st** – stipes; **stp** – stipital process.

distally; the proximal palpomere is especially narrow basally as it is squeezed between prementum and labrum when the mouthparts are retracted, leaving only the apical palpomere visible (Fig. 7A); the base of the spindle-shaped apical palpomere is slightly curved mediad; it bears a medium length seta at mid-level, a long seta apically, and a short one sub-apically. The glossa, placed far behind the distal premental margin (gl, Fig. 8C - E), consists of a rather narrow base and a broad lobe; the latter is set with rows of curved microtrichia (Fig. 5B), resulting in a mushroom-like appearance in lateral view; the extended surface between the glossal base and the distal premental margin is stabilized by the massive ventral glossal sclerite (glvs, Fig. 5B); ligamentous projections extend laterally into the ventral region of the glossa from the ventral sclerite; the similarly massive dorsal glossal sclerites (glds, Fig. 5B) stabilize especially the narrow base of the glossa. The basiparaglossal brushes (bpb, Figs. 5E; 8D, E) are well-developed, but paraglossae are not recognizable. The salivarium (sv, Figs. 5B; 8B) between glossa and distal hypopharynx is stabilized by a long U-shaped sclerite ventrally and on the dorsal side by two longitudinally oriented sclerotized bars, which posteriorly fuse with the hypopharyngeal buttons. The salivary duct (svd, Fig. 8A, B) is relatively thick, especially its posterior portion; it forms a large, dorsally directed loop directly anteriad the suboesophageal ganglion. The thin premental arms (pma, Figs. 5C; 8D) are connected to the well-developed hypopharyngeal rods (hyb, Fig. 5C) which stabilize the distal hypopharynx laterally. The distal hypopharynx (dhy, Figs. 5B, C; 8D, E) is continuous with the large infrabuccal pouch (ibp, Figs. 5B, C; 9D), which was deflated and almost empty in the µ-CT scanned specimen; the small amount of material it contained partly appeared like compacted small pieces of cuticle, judging from shape and histological staining; a pattern of dorsal folds indicates that the pouch can be inflated depending on feeding status.

Musculature (Fig. 8A, B): Musculus tentoriopraementalis (0la5): O: partly on posterior tentorial arm and partly on ventral head capsule close to occipital foramen; **I:** tendons of the two sides fusing into one that inserts on the proximal premental margin. **M. praementoparaglossalis (0la11):** absent. **M. praementoglossalis (0la12): O:** distal part of the ventral premental face; **I:** base of the dorsal glossal wall / sclerite. **M. praementopalpalis externus (0la14):** very thin muscle; **O:** premental arm; **I:** base of the proximal palpomere. **M. palpopalpalis labii primus / secundus (0la16 / 17):** absent / not recognizable. **M. tentoriohypopharyngalis (0hy3): O:** posterior tentorial arm and small part of

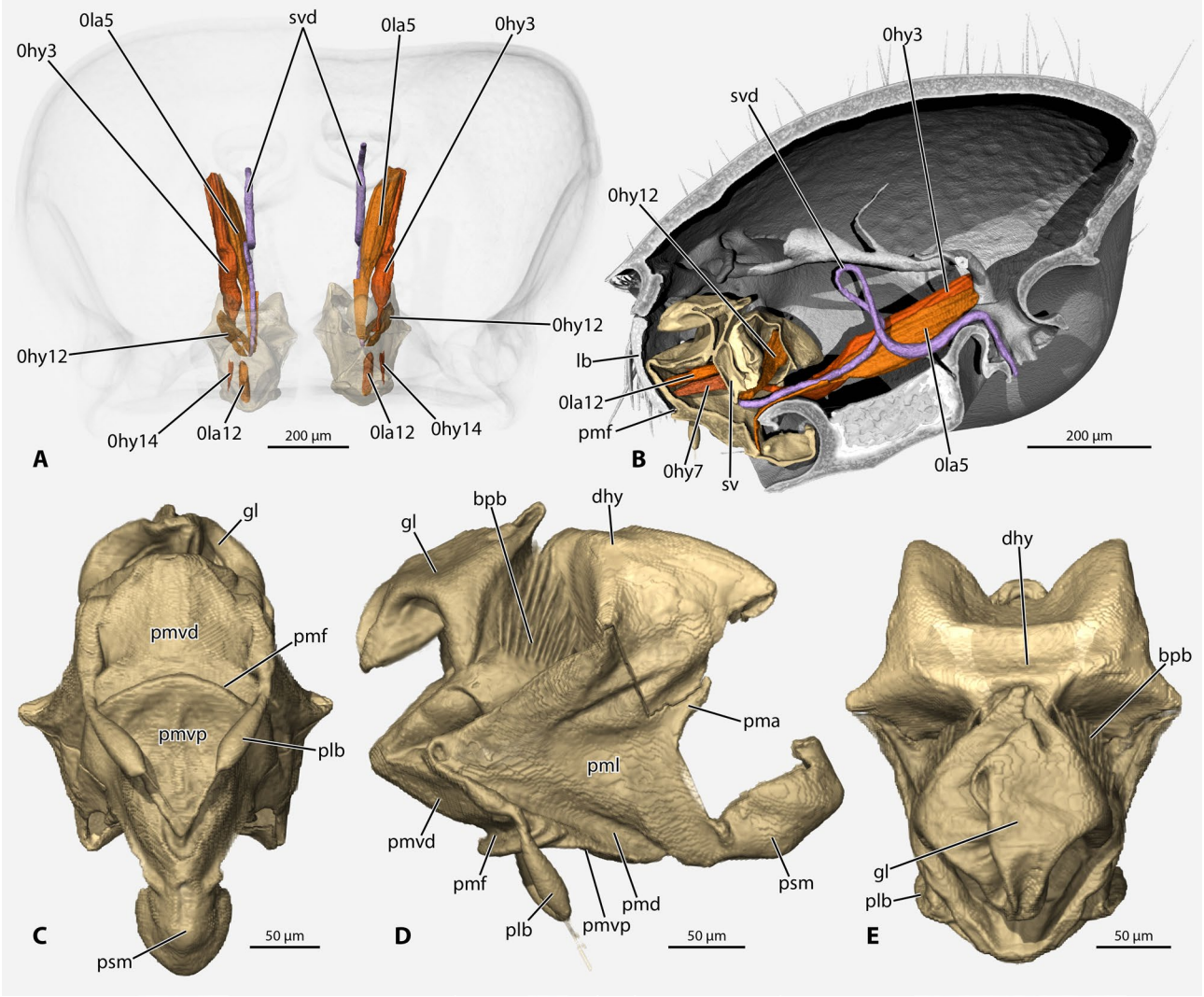

Fig. 8: Volume renderings of the labium and labial musculature of *Tatuidris tatusia*, based on micro-computed tomography scan. **A, B:** Labial muscles and salivary duct. **A:** Dorsal view left, ventral view right. **B:** Sagittal view. **C - E:** Details of the labium. **C:** Frontal view. **D:** Lateral view. **E:** Dorsal view. **Abbreviations: 0hy3** – M. tentoriohypopharyngalis; **0hy7** – M. praementosalivarialis; **0hy12** – M. hypopharyngosalivarialis; **0la5** – M. tentoriopraementalis; **0la12** – M. praementoglossalis; **0la14** – M. praementopalpalis externus; **bpb** – basiparaglossal brush; **dhy** – distal hypopharynx; **gl** – glossa; **lb** – labrum; **plb** – labial palp; **pmd** – premental ditch; **pmf** – premental furrow; **pml** – lateral premental surface; **pmvd** – distal ventral premental surface; **pmvp** – proximal ventral premental surface; **psm** – postmentum; **sv** – salivarium; **svd** – salivary duct.

the head capsule laterad 0la5; **I:** hypopharyngeal button. **M. praementosalivarialis (0hy7): O:** distal premental part proximad 0la12; **I:** ventrally on the sclerotized salivarium. **M. hypopharyngosalivarialis (0hy12): O:** dorsolaterally from the stabilizing sclerites of the distal hypopharynx (hypopharyngeal rods); **I:** dorsally and laterally on the salivarium.

Labrum and distal epipharynx

The labrum is a trapezoidal plate with almost straight, distally converging lateral edges (Fig. 7C); at full closure, it is nearly vertically oriented (assuming a prognathous head, Fig. 7B); its distal margin is concave and thus appears bilobed (Fig. 7A, C, E). The proximolateral labral processes (lbrp, Fig. 7B, D, E) are large, lobe-like, and about half as long as the entire labrum; when the mouthparts are retracted, the distal processes of the external stipital sclerites push against the proximolateral labral processes (Fig. 7B); this interlocking mechanism and the tight fit of the labral margin in the premental and stipital grooves lead to tight closure of the buccal cavity (Fig. 7A). The external surface of the labrum is densely covered with thick, long, and apicomedially directed setae (Fig. 7C); they are distributed across most of the surface apart from the distal margin and a triangular distal medial area; the setae decrease in length from the base to the apex of the labrum and are most densely set apicolaterally. The proximal internal margin of the labrum is continuous with the flexible distal epipharynx (ep, Fig. 9A, D), which is slightly longer than the labrum; this anteriormost portion of the

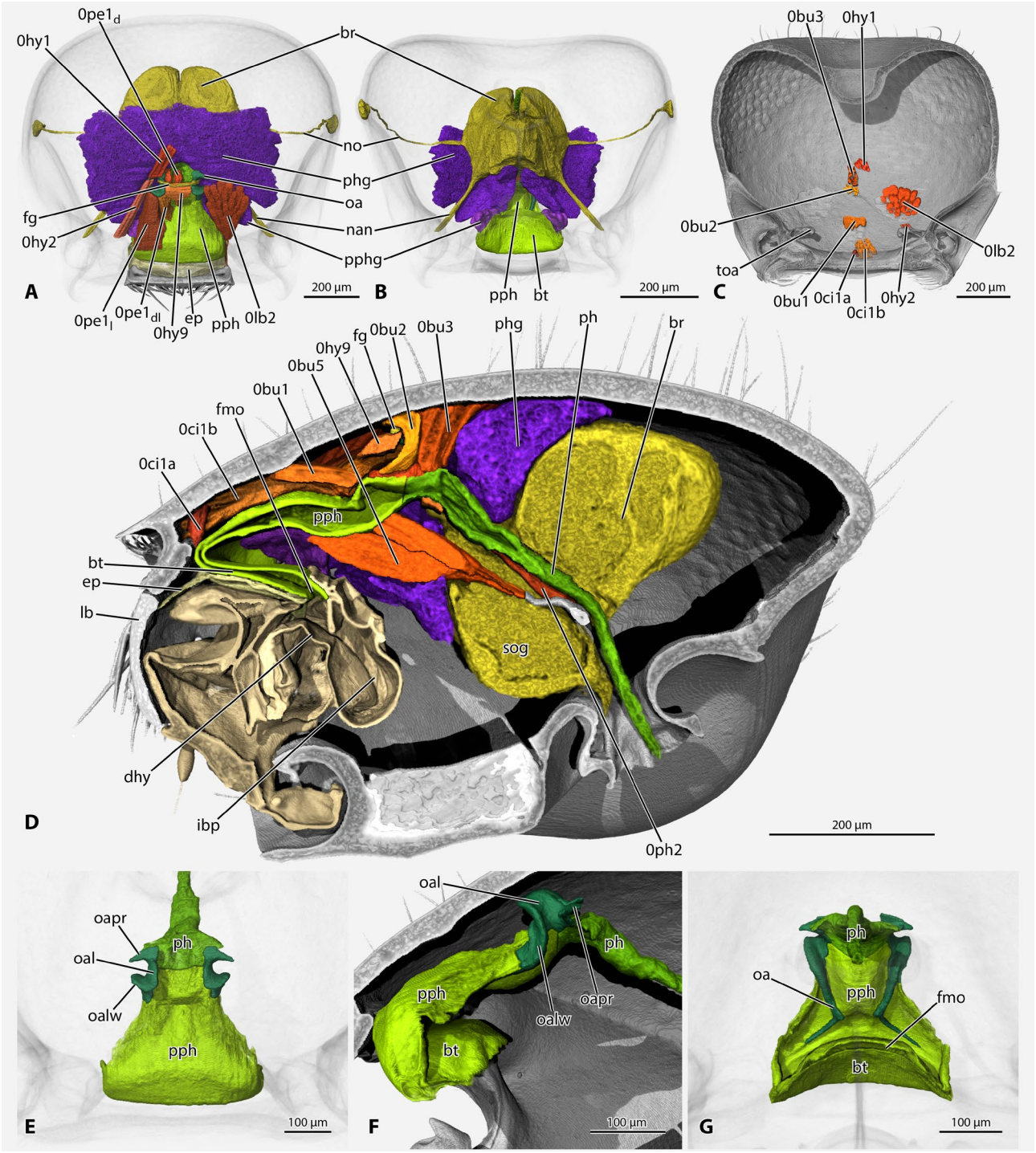

Fig. 9: Volume renderings of the digestive tracts, its muscles and glands, and the central nervous system of *Tatuidris tatusia*, based on micro-computed tomography scan. **A:** Dorsal view of digestive tract, select muscles, glands, and the nervous system. **B:** Ventral view of digestive tract, glands, and nervous system. **C:** Ventral view of cut open head capsule showing dorsal head muscles. **D:** Sagittal view of digestive tract, muscles, glands, and nervous system. **E - G:** Distal digestive tract with focus on prepharynx and oral arms. **E:** Dorsal view. **F:** Lateral view. **G:** Posteroventral view. **Abbreviations: 0bu1** – M. clypeobuccalis; **0bu2** – M. frontobuccalis anterior; **0bu3** – M. frontobuccalis posterior; **0bu5** – M. tentoriobuccalis posterior; **0ci1a** – M. clypeopalatalis, unpaired portion; **0ci1b** – M. clypeopalatalis, paired portion; **0hy1** – M. frontooralis; **0hy2** – M. tentoriooralis; **0hy9** – M. oralis transversalis; **0lb2** – M. frontoepipharyngalis; **0pe1$_d$** – M. pharyngoepipharyngalis, dorsal portion; **0pe1$_{dl}$**– M. pharyngoepipharyngalis, lateral dorsal portion; **0pe1$_l$** – M. pharyngoepipharyngalis, lateral portion; **0ph2** – M. tentoriopharyngalis; **br** – brain; **bt** – buccal tube; **dhy** – distal hypopharynx; **ep** – epipharynx; **fg** – frontal ganglion; **fmo** – functional mouth opening; **ibp** – infrabuccal pouch; **lb** – labrum; **nan** – antennal nerve; **no** – optical nerve; **oa** – oral arm; **oal** – oral arm lamella; **oalw** – oral arm lateral wall; **oapr** – oral arm process; **ph** – pharynx; **phg** – pharyngeal gland; **pph** – prepharynx; **pphg** – prepharyngeal gland; **sog** – suboesophageal ganglion; **toa** – torular apodeme.

cibarium is followed by the anterior / upper wall of the long buccal tube.

Musculature (Fig. 9A, C): Musculus frontoepipharyngalis (M. 9 / 0bl2): O: frontal area shortly posteriad the antennal bases, laterad 0bu1 and 2; **I:** upon a thin, long tendon attached at the lateral inner corners of the labrum.

Cephalic digestive tract

The anterior prepharynx (pph, Fig. 9A, B, D - G), especially the region of the buccal tube (bt, Figs. 5D; 9B, D, F, G), is broad, about 4 / 7 as wide as the minimum width of the head capsule internally (e.g., Fig. 9A, B); it narrows gradually to slightly less than half this width towards the pharynx (Fig. 9E). The dorsal (epipharyngeal) prepharyngeal wall (dw, Fig. 5F) is partially robust, with a maximum thickness of about 11 µm in the region around the insertion site of muscle 0ci1b and a minimum of about 2 µm in the buccal tube close to the functional mouth opening (fmo, Figs. 5F; 9G); with about 7 µm thickness, the ventral (hypopharyngeal) wall of the prepharynx (vw, Fig. 5F) is slightly thinner throughout its length. The hypopharyngeal wall of the buccal tube is covered with scale-like, flat ridges set with microtrichia (ca. 4 µm), with increasing length (up to ca. 10 µm) towards the functional mouth opening (hym, Fig. 5F); the dorsal (epipharyngeal) wall is set with thin, short microtrichia (ca. 2 - 3 µm); longer microtrichia (up to ca. 8 µm) are only present on the wrinkled epipharyngeal wall, forming a lip-like structure close to the functional mouth opening (epm, Fig. 5F); the tip of the lip bears a brush of longer microtrichia (ca. 15 - 20 µm, eplm, Fig. 5F) on its central area. To stabilize the broad distal part of the prepharynx, the oral arms diverge distally, appearing as mirrored angle brackets (><) on the ventral (hypopharyngeal) wall (oa, Fig. 9G); the proximal part of the oral arms, close to the anatomical mouth opening / frontal ganglion, curves sharply upward (Fig. 9F); this curved part forms a broad, concave lateral wall (oalw, Fig. 9E, F) and is continuous with broad dorsal plates, the oral arm lamellae (oal, Fig. 9E, F); posteriorly, the plates are extended as short, laterally diverging processes (oapr, Fig. 9E, F).

Musculature (Fig. 9A, C, D): Musculus frontooralis (0hy1): O: centrally in the frontal region (Fig. 9C); **I:** posteriorly on the oral arm process (Fig. 9A). **M. tentoriooralis (0hy2):** almost twice as long as 0hy1; **O:** on the base of the torular apodeme (Fig. 9C); **I:** anteriorly on the oral arm process (Fig. 9A). **M. oralis transversalis (0hy9):** transverse muscle of the prepharynx, connecting the oral arm lamellae of both sides (Fig. 9A, D); a second, smaller transverse muscle bundle is also present on the ventral side of the pharynx at the level of 0bu3 (Fig. 9D). **M. clypeopalatalis (0ci1):** two distinct parts: **0ci1a:** very small, unpaired muscle; **O:** anteriorly on the clypeus (Fig. 9C); **I:** buccal tube close to the functional mouth (only partly visible in 3D reconstruction due to minute muscle size). **0ci1b:** distinctly larger than 0ci1a and paired; **O:** lateral region of the clypeus (Fig. 9C); **I:** along a long area of the thickened dorsal prepharyngeal wall (Fig. 9D). **M. clypeobuccalis (0bu1):** flattened but broad muscle; **O:** on cuticular swelling likely corresponding to epistomal sulcus (Fig. 9C, D); **I:** on posterior wall of dorsal prepharyngeal depression (Fig. 9D). **M. frontobuccalis anterior (0bu2): O:** frontal area at the level of the frontal ganglion (Fig. 9C, D); **I:** dorsal prepharyngeal wall at the level of the frontal ganglion, curving around it (Fig. 9D). **M. frontobuccalis posterior (0bu3): O:** frontal area directly behind 0bu2 (Fig. 9C, D); **I:** directly behind 0bu2 but straight, not curved (Fig. 9D). **M. tentoriobuccalis anterior (0bu5) (**& possibly **posterior, 0bu6):** two closely set bundles that either represent the anterior and posterior tentoriobuccal muscle or just the anterior one that is slightly separated in two parts; **O:** anteromedian process of the tentorial bridge (Fig. 9D); **I:** ventral prepharyngeal wall anteriad of 0bu2 / the anatomical mouth (Fig. 9D). **M. pharyngoepipharyngalis (0pe1):** well-developed longitudinal musculature of the prepharynx. The main lateral bundles ($0pe1_l$, Fig. 9A) connect the concave lateral walls of the oral arms and the anterior prepharynx close to the buccal tube, the much smaller median bundles ($0pe1_{dl}$, Fig. 9A) connect the dorsal oral arm lamellae and the central prepharynx. The unpaired dorsal bundle ($0pe1_d$, Fig. 9D) is short and extends from the pharynx around the level of 0bu3 to the prepharynx around the level of 0bu1.

Cephalic glands

The mandibular gland consists of a moderately sized, drop-shaped reservoir (Fig. 4A, B) that is cupped by round to oval glandular cells with a diameter of around 20 - 25 µm (mdgc, Fig. 10A, B). The short gland duct enters the mandibular base and opens on the mandalus (ma, Fig. 4C, 5A). The inner mandibular gland, first described by Billen & Delsinne (2014), is formed by spherical secretory cells with a diameter of 25 - 30 µm that occupy most of the mandibular lumen (mdig, Fig. 10C, D). Each cell is connected to a duct cell, and all ducts form a bundle that opens to the exterior through a sieve plate at the ventroproximal inner side of the mandible (mdigo, Fig. 10D). The pharyngeal gland is the largest gland of the head (phg, Fig. 9A, B, D); it opens into the pharynx close to the anatomical mouth opening (phgo, Fig. 10E) and consists of a large sack of glandular epithelium with a thickness of about 10 - 20 µm (Fig. 10F); its anterior lobes extend ventrally into the space between the brain, the infrabuccal pouch, and the prepharyngeal gland (Fig. 9D); the posterior lobes almost completely cover the brain dorsally (Figs. 9A; 10F). The prepharyngeal gland (pphg, Figs. 9A, B; 10G, H) forms two paired clusters of large cells laterad and below the anterior prepharynx. The round cells have a diameter of 50 - 60 µm and are filled with numerous secretory vesicles that stain darkly in histological preparation and most likely contain digestive enzymes. Their accompanying ducts (pphgc, Fig. 10G, H) open through a small sieve plate in the buccal tube close to the functional mouth opening (pphgo, Fig. 10H).

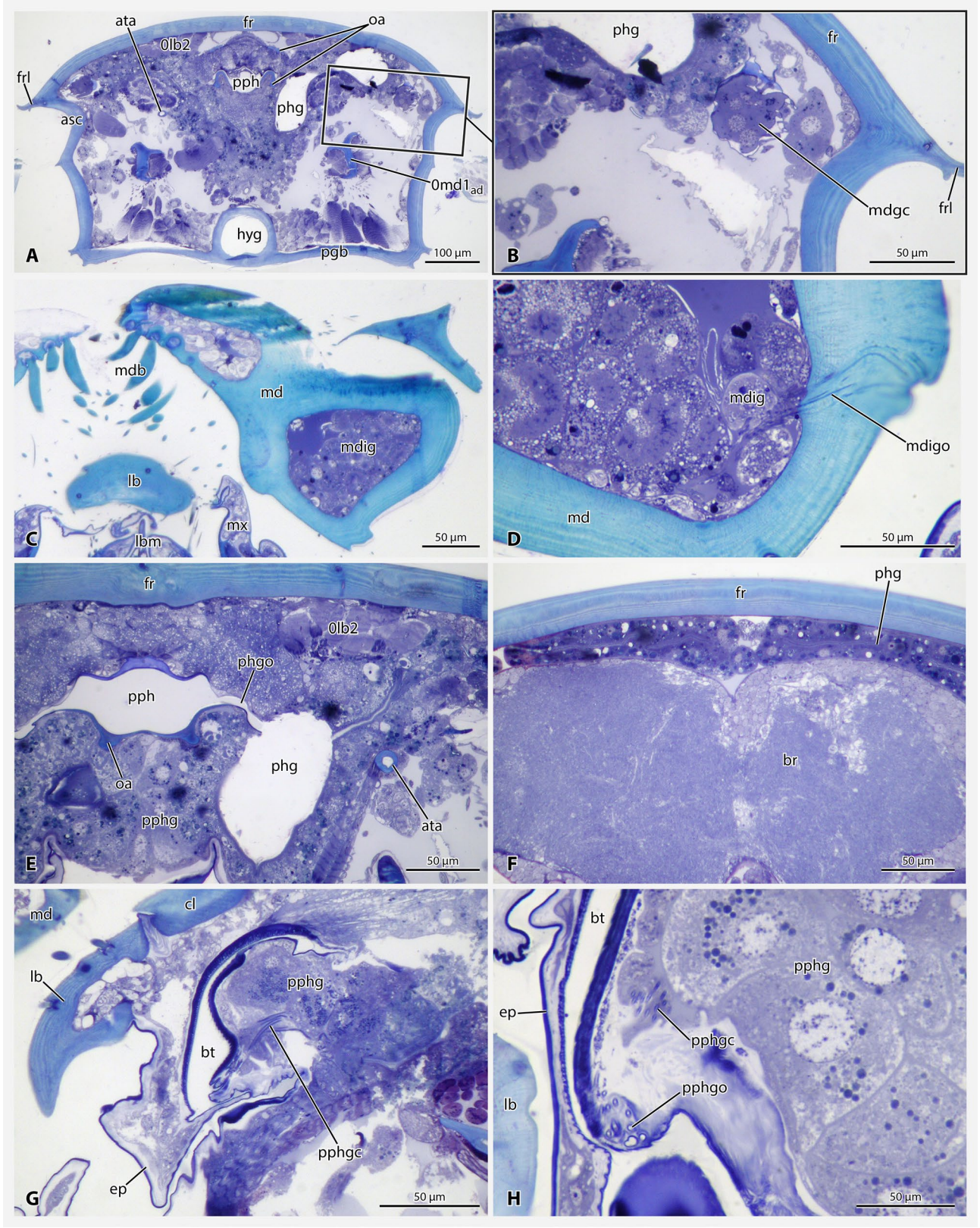

Fig. 10: Histological sections through the head of *Tatuidris tatusia*. **A - F, H:** Cross sections. **G:** Longitudinal section. **A:** Overview section showing position of the mandibular gland. **B:** Enlarged box from A. **C:** Overview of the mandible showing inner mandibular gland. **D:** Detail of the inner mandibular gland opening. **E:** Opening region of the pharyngeal gland. **F:** Posterior region of the pharyngeal gland and brain. **G:** Anterior digestive tract with prepharyngeal gland. **H:** Detail of the prepharyngeal gland opening. **Abbreviations: 0lb2** – M. frontoepipharyngalis; **$0md1_{ad}$** – M. craniomandibularis internus apodeme; **asc** – antennal scrobe; **ata** – anterior tentorial arm; **br** – brain; **bt** – buccal tube; **cl** – clypeus; **ep** – epipharynx; **fr** – frontal area; **frl** – frontal lobe; **hyg** – hypostomal groove; **lb** – labrum; **lbm** – labium; **md** – mandible; **mdb** – mandibular chaetae brush;

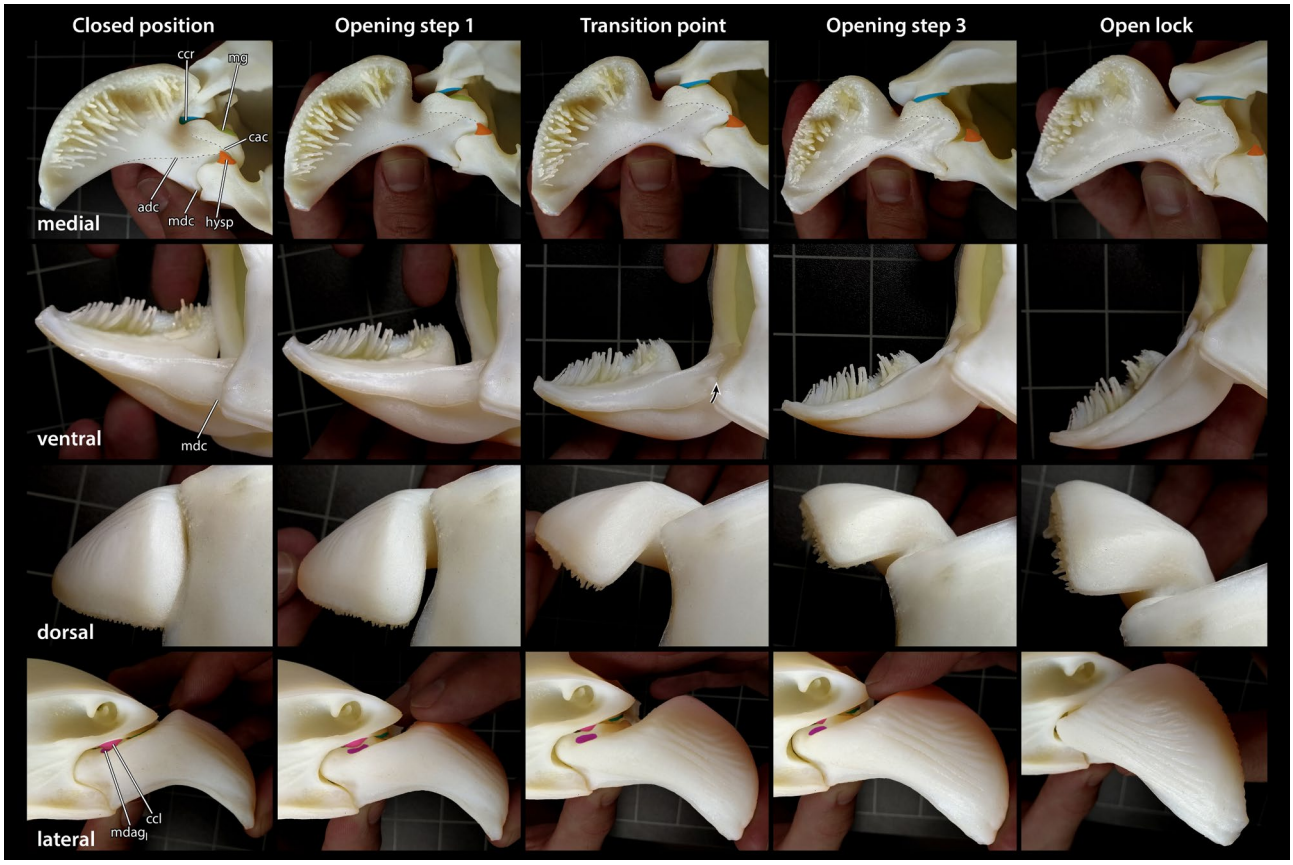

Fig. 11: Photographs of the 3D-printed model of the head capsule and mandible of *Tatuidris tatusia*, showing our hypothesis for the mandible opening motion based on physical experiments with the model. We show the motion in medial (upper row), ventral (second row), dorsal (third row), and lateral (last row) view. Images were taken in Closed position (first column); Opening step 1 (second column), in which the mandible performs an upward / outward rotation based on sliding of the dorsal mandibular stem along the clypeal condylar ridge, the canthellar groove along the hypostomal process, the lateral mandibular acetabular groove along the clypeal condylar lobe and the mandibular condyle mesially along its articulatory fossa; the Transition point (third column) is reached when the clypeal rail sits in the medial mandibular groove, the canthellar groove loses contact with the hypostomal process, the mandibular condyle rests in its mesal position (black arrow in ventral view), and the condylar lobe sits on top of the ridge separating medial and lateral articulatory grooves; in Opening step 3 (fourth column), the mandible rotates outward and reaches its Open lock state (fifth column) as the clypeal condylar lobe completely locks into the medial mandibular acetabular groove. **Abbreviations: ccl** – clypeal condylar lobe; **ccr** – clypeal condylar rail; **adc** – adductor carina; **cac** – canthellar carina; **hysp** – triangular hypostomal process; **mdag$_l$** – lateral mandibular acetabular groove; **mdc** – mandibular condyle; **mg** – medial mandibular groove. **Color marking:** cyan – clypeal condylar rail; green – medial mandibular; orange – triangular hypostomal process; pink – clypeal condylar lobe; purple – lateral mandibular acetabular groove.

Possible mandibular motions

Mandibular opening has never been directly observed or documented in living *Tatuidris tatusia*. However, via manipulation of a 3D-printed model of the head capsule and mandible, we found that the mandible fits tightly into the cranial contact surfaces, from the closed to the fully open posture. Because of this tight fit, we hypothesize here a mode of motion for the mandible based on our handling of the model (Fig. 11). It should be noted that this is a preliminary interpretation that does not account for soft structures and does not represent a precise kinematic assessment of mandibular movement. Moreover, a mechanical model has not been proposed for more "generalized" ants, thus the extendibility of our observations to other genera and subfamilies must be approached with caution, particularly given the derived nature of the mandibular articulations. To replicate our manipulations, we have provided our model as supplementary material for 3D printing (Zenodo DOI: 10.5281/zenodo.6046240).

mdgc – mandibular gland cells; **mdig** – inner mandibular gland; **mx** – maxilla; **oa** – oral arm; **pgb** – postgenal bridge; **phg** – pharyngeal gland; **pph** – prepharynx; **phgo** – prepharyngeal gland opening; **pphg** – prepharyngeal gland; **pphgc** – prepharyngeal gland canals; **pphgo** – prepharyngeal gland opening.

With the caveats mentioned above, we observe that the tight fit highly constrains the range of motion of the mandible, revealing that two axes of rotation are required to obtain maximal gape (~160°) and that the opening motion has three phases. The first phase of opening, starting with the mandible at closure and comprising the first axis of motion, is an outward and upward (dorsal) rotation where the masticatory margin becomes dorsomedially directed from its medially directed position at full closure. The second phase is a distinct and stable transition point. The third phase, comprising the second axis of motion, is a posterolateral swing, which continues to the point where the mandible physically cannot be opened further. At this maximal gape, the masticatory margin is directed almost completely anteriad. The first and third phases are each structured by a separate mechanism, which must be physically engaged in order to guide the mandibular motion. Neither mechanism is engaged during the second phase, which is transitional, and mandibular motion cannot be made from the transition point without engaging one or the other mechanism.

Mechanically, **Phase I** is defined by a tricondylic pivot-slide articulation with three main components: a pivot and paired lateromedial rail systems. The *pivot* is formed by the primary (ventral) mandibular condyle, which fits in the deep and narrow cranial fossa and which has a limited degree of lateromedial motion therein (see black arrow, Fig. 11 mesal view, transition point). The slide is dicondylic, comprising the medial and lateral rail systems: The medial rail is formed by the canthellar carina of the mandible (cac, Fig. 11 medial view), which slides along the inner hypostomal carina to the point of transition; the lateral rail is formed by the condylar lobe of the cranium (ccl, Fig. 11 lateral view), which slides from the lateral acetabular groove ($mdag_l$, Fig. 11 lateral) onto the pyramidal ridge of the mandible that separates the medial and lateral acetabular grooves. When the lateromedially paired rails are at the limit of their contact from Phase I and before the mechanism of Phase III engages, the mandible is at a stable point of transition, with very little play in its socket, which we consider to be **Phase II**.

Phase III is a complex tongue-and-groove sliding-hinge articulation with a lateral stop mechanism at maximum gape. The dicondylic sliding hinge is formed ventrally by the primary mandibular condyle and dorsally by the tongue-and-groove mandibulocranial articulation. While the primary condyle simply pivots in its fossa, the medial groove of the mandible (mg, Fig. 11 medial view) engages with the condylar rail of the clypeus (ccr, Fig. 11 medial view) and guides the mandible to its maximal gape. Upon reaching the maximal gape, the mandible is stopped by the lateral condylar lobe (ccl, Fig. 11 lateral view), which itself fits tightly into the median acetabular groove of the mandible, preventing lateral or posterior overextension. The closure of the mandible is a complete reverse of this sequence. At total closure, the basal margin of the mandible contacts the inflected surface of the clypeal groove, another potential stop mechanism. Because Phases I and III represent two axes of movement that are part of one continuous range of motion, punctuated by Phase II, the motion of the mandible may be conceived of as a "wandering axis" that is constrained by four condyles, of which three are transitional while only the primary condyle is fixed.

Morphology of *Tatuidris tatusia* compared with other Poneria

Our comparative morphological observations of the worker caste across Poneria are summarized in Table 2 and Figures 12 - 17. The polarities of the mapped characters were reasoned based on the principle of parsimony across the preexisting topologies of Poneria (Romiguier & al. 2022), Ponerinae (Branstetter & al. 2017, Borowiec & al. 2019, Branstetter & Longino 2022), Amblyoponinae (Ward & Fisher 2016), and Proceratiinae (Borowiec & al. 2019), with groundplan conditions inferred from Richter & al. (2022) and Boudinot & al. (2022a). Inferences about mouthpart polarities and internal structures are limited by the availability of fine anatomical data such as the SEM images from Keller's (2011) atlas and completed µ-CT studies of head anatomy (Richter & al. 2019, 2020, 2021a, 2022, also Hita Garcia & al. 2019 for external features of *Discothyrea*). In this respect, the observations are biased toward *Tatuidris tatusia* and those taxa for which we have 3D renders. We have not considered †*Eulithomyrmex* in the present comparisons as this compression fossil has inadequate preservation of structural detail for meaningful interpretation, at least given the currently available documentation (Carpenter 1930 and specimen UCM17019 on AntWeb 2022). Future work on ponerine anatomy will absolutely advance the knowledge of this clade, particularly through focused sampling of *Apomyrma*, *Ankylomyrma*, and *Paraponera*, as well as the morphologically highly modified ponerines, such as *Harpegnathos*, *Thaumatomyrmex*, and the genera of the *Plectroctena* clade.

Across Poneria, we tabulated 92 apomorphies (Tab. 2). Of these, we counted 47 unambiguous and 13 ambiguous autapomorphies, with the latter accounting for uncertainty due to limited sampling (Fig. 12). The 13 ambiguous autapomorphies are restricted to *Tatuidris tatusia*. Considering only unambiguous conditions, *T. tatusia* has both the most total apomorphies and the most autapomorphies, with 29 and 15, respectively (Figs. 13 and 14). The taxa with the next greatest number of apomorphies based on our present tabulation are *Apomyrma stygia*, *Ankylomyrma coronacantha*, and *Paraponera* (*Paraponera clavata* + †*Paraponera dieteri*), which have 17, 16, and 12 apomorphies and 9, 5, and 4 autapomorphies, respectively (Figs. 15 - 17). Of the clades with > 100 species, Amblyoponinae is the clade with the most derived features (7 apo-, 4 autapomorphies), followed by Proceratiinae (2 apomorphies, 1 autapomorphy).

We observe that Ponerinae is poorly defined morphologically, having no known unambiguous autapomorphies based on our assessment. For the two synapomorphies of this subfamily as recognized by Bolton (2003) –

Tab. 2: Summary matrix of numbered apomorphies, based on the female castes, which are presented as a hypothetical transformation series in Figure 12 in order to sense the relative number of derivations in ponerine lineages. The presented characters emphasize the cranium. Ground plan conditions drawn from the estimates of Boudinot & al. (2022a) and Richter & al. (2022), following up on the intuition-based hypotheses of Bolton (2003). Characters and synapomorphies for Ponerinae, Amblyoponinae, and several for the Apomyrminae are drawn from Bolton (2003), Keller (2011), Boudinot (2015), and Boudinot & al. (2022a), which are abbreviated as "B03", "K11", "B15", and "B22" below; other characters were composed and scored based on the present study. Due to the limited availability of completed micro-computed tomography (μ-CT) studies and scanning electron microscopy (SEM)-imaged specimens, this list is largely restricted to external features. Also note that this is not an exhaustive list of apomorphic conditions in the Poneria, and that not all conditions are illustrated. Note further that our sampling may miss subfamilial variation for some characters due to these limitations. While this level of variation would be unlikely to change our inferences for deeper nodes, a more complete and formal reconstruction – outside the scope of this contribution – may refine evolutionary interpretations. We reiterate that our sampling is limited, especially for the mouthparts, thus future studies would benefit from systematic evaluation using SEM and μ-CT. # = number, Po = Ponerinae, Ap = Apomyrminae, Am = Amblyoponinae, *Pa* = *Paraponera*, Pr = Proceratiinae, *An* = *Ankylomyrma*, *Ag* = †*Agroecomyrmex*, *Ta* = *Tatuidris*, 1 = state TRUE, 0 = state FALSE, - = state inapplicable, ? = state uncertain, (#) = state known to be reversed within taxon, 0 / 1 = variation between states observed, 0 / ? = state 0 observed but state 1 not ruled out for all taxa, 1 / ? = state 1 observed but state 0 not ruled out for all taxa. State 1 is used here for the reasoned apomorphic condition in the context of the Poneria.

#	Definition	Po	Am	Ap	*Pa*	Pr	*An*	*Ag*	*Ta*
1–2: Possible synapomorphies of Ponerinae									
1	Frontal carinae and medial torular arches at least partly "fused" (B03)	1	1	0	0	0	0	0	0
2	Frontal carinae / torular arches forming lobes which distinctly curve posteromedially, thus with "pinched" appearance (B03)	1(0)	0/1	0	0	0(1?)	0	0	0
3: Possible synapomorphy of Agroecomyrmecinae, also for Amblyoponinae plus Apomyrminae									
3	Eyes situated in extreme posterior portion of head (B15, B22)	0(1)	0/1	1	0	0	1	1	1
4–6: Possible synapomorphies of Amblyoponinae plus Apomyrminae									
4	Mandible not shovel-shaped (= "triangular") (*sensu* Richter & al. 2022) (B22)	0(1)	1	1	0	0	0	0	0
5	At least one tooth occurring on mandibular basal margin (B22)	0(1)	0/1	1	1	0	0	0	0
6	Labrum with chaetae ("dentiform" or "traction setae") (B22)	0	0/1	1	0	0	0	0	0
7–13: Apomorphies or possible synapomorphies of Amblyoponinae									
7	Mandibles elongate thus relatively bar-shaped, e.g., *Stigmatomma* (B22)	0(1)	1/0	0	0	0	0	0	0
8	Mandibular teeth large and triangular, fang-like in the form of, e.g., *Stigmatomma* rather than *Belonopelta* (B22)	0	1/0	0	0	0	0	0	0
9	Anterior clypeal margin with chaetae (B03, K11, B15, B22)	0	1(0)	0	0	0	0	0	0
10	Genal region with anterolateral spines (note 1) (B22)	0	1/(0)	0	0	0	0	0	0
11	Petiolar tergum without distinct posterior face (B03, B22)	0	1	0	0	0/1	1	0	0
12	Helcium weakly constricted posteriorly (B03, B22)	0	1	0	0	0/1	0	0	0
13	Helcium supraaxial relative to a line drawn through the midheight of the segment (K11, B22)	0	1	0	0	0/1	0	?	1

[1]. *Probolomyrmex* has antennal toruli that are directed dorsally rather than laterally, but these structures are close-set, being only separated by the median longitudinal carina / lamina, whereas those of *Apomyrma* are wideset.

#	Definition	Po	Am	Ap	*Pa*	Pr	*An*	*Ag*	*Ta*
14–27: Possible synapomorphies of Apomyrminae									
14	Median portion of clypeus raised and pyramidal (B15, B22)	0	0	1	0	0	0	0	0
15	Frontal carinae absent (B15, B22)	0	0	1	0	0	0	0	0
16	Antennal toruli wideset and directed dorsally rather than laterally (B03, K11, B22) (see note 1)	0	0	1	0	0	0	0	0
17	Propleurae bulgingly muscular, i.e., strongly convex and clearly visible in lateral view (B15)	0/1	0/1	1	0	0/1?	0	0	0
18	Promesonotal articulation modified, hyperflexible (B03, B15, B22)	0	0	1	0	0	0	0	0
19	Propodeal lobes absent (B03, B15, B22) (see note 2)	0	0	1	0	0	0	0	0
20	Petiolar tergum forming a pedunculate collar around segment anteriorly, restricting sternite to small posterior plate surrounded by two flat lobes that are sutured anteroventromedially	0	0	1	0	0	0	0	0
21	Petiolar node subrectangular, resembling a rounded inverted trapezoid (see Fig. 17)	0	0	1	0	0	0	0	0
22	Helcium infraaxial relative to a line drawn at segment midheight (B22)	0/1	0	1	0	0	1	?	0
23	Abdominal segment III spiracles directed ventrad due to bulging of the segment over the helcium (B03) (see also Bolton 1990)	0	0	1	0	0	0	0	0
24	Abdominal tergum III fused posteroventrad helcium, thus transverse sulcus present on ventral surface (B03, K11, here)	0	0	1	0	0	0	?	0
25	Prora of abdominal sternum III absent (B22)	0/1	0/1	1	0	0	?	1	0
26	Abdominal segment IV not tubulated (B22)	0	0/1	1	0	0	?	?	0
27	Presclerites of abdominal segment IV unconstricted (B03, B22)	0/1	0/1	1	0	0	0	0	0
28, 29: Possible synapomorphies of Paraponerinae, Proceratiinae, Agroecomyrmecinae									
28	Promesonotal articulation fused, prothorax immobile (see notes 3, 4)	0	0	0	1	1	1	1	1

[2]. While *Apomyrma* appears to have propodeal lobes, these may be seen to be the posterolateral corners of the metapleural region, rather than ventrolateral lobate processes of the carina bordering the propodeal foramen. That is, the apparent lobes of *Apomyrma* are the "posterolateral process of the metapleural gland orifice" (mpgop) rather than the "lateral lobe of the propodeal foramen" (prffl) of Lieberman & al. (2022: fig. 4).

[3]. Two conditions previously used for subfamilial and tribal diagnosis by Bolton (2003) can now be reasonably polarized, that of promesonotal and petiolar fusion (for the latter, see note 5 below). Fusion of the promesonotal articulation is an apomorphy shared by Paraponerinae, Proceratiinae, and Agroecomyrmecinae, while loss of the promesonotal suture is an apomorphy shared by Proceratiinae and Agroecomyrmecinae; this articulation is unsutured and capable of flexion in Ponerinae, Amblyoponinae, and Apomyrminae. In contrast to Paraponerinae, the metanotal spiracle is lost in Proceratiinae and Agroecomyrmecinae, which have complete mesosomal fusion. Loss of the promesonotal suture gives the mesosoma of these two subfamilies a dome-shaped appearance, with elongation of the mesosoma resulting in a tubular shape in *Probolomyrmex*. We expect that the compaction of the mesosoma conceals additional, internal synapomorphies of Paraponerinae, Proceratiinae, and Agroecomyrmecinae. See note 4 below for more structural detail about the promesonotal suture.

[4]. When the pro- and mesonota are fused, the promesonotal suture forms. This suture passes from the posterolateral corner of the pronotum through the mesothoracic (anterior) spiracle of one side over the mesosomal dorsum and down through the spiracle of the other side to the corner. The spiracle, therefore, divides the suture into dorsal and ventral portions. The dorsal portion is obliterated in both Proceratiinae and Agroecomyrmecinae, while the ventral portions are retained in the latter and obliterated in the former.

#	Definition	Po	Am	Ap	*Pa*	Pr	*An*	*Ag*	*Ta*
29	Petiole with complete tergosternal fusion (see note 5)	0	0	0	1	1?(0)	1	?	1
30–36: Possible synapomorphies of Paraponerinae									
30	Scrobe developed, capable of receiving scape and flagellum	0	0	0	1	0	1	1	1
31	Body size large, i.e., head width > 3.5 mm (see Breed & Harrison 1985)	0/1	0	0	1	0	0	0	0
32	Scrobe above/ mediad compound eye	0	0	0	1	0	0	0	0
33	Paramedian clypeal processes and lateral notches developed	0/1	0	0	1	0	0	1	0
34	Paired pronotal tubercles developed	0(1)	0	0	1	0	1	1	0
35	Tibiae rectangular in cross-section, tarsomeres widened, tarsomeres II–V covered ventrally with dense setal brushes	0	0	0	1	0	0	0	0
36	Petiole hatchet-shaped, i.e., pedunculate and with angular anterodorsal corner of the node (B03, B15)	0	0	0	1	0	0	0	0
37, 38: Possible synapomorphies of Proceratiinae plus Agroecomyrmecinae									
37	Mesosomal segments completely fused, promesonotal suture absent or vestigial and metanotal spiracle vestigial or absent (see notes 3, 4)	0	0	0	0	1	1	1	1
38	Abdominal tergum IV strongly vaulted (see note 6 and Figs. 13, 16, 17)	0/1	0	0	0	1(0)	1	1	1
39, 40: Possible synapomorphies of Proceratiinae									
39	Toruli situated near to (touching) or exceeding anterior clypeal margin	0/1	0/1	0	0	1	0	0	0
40	Ventral promesonotal suture, completely fused (externally obliterated or sulcate) ventrad the anterior/ mesothoracic spiracle (see note 4)	0	0	0	0	1/0	0	?	0
41–44: Possible synapomorphies of Agroecomyrmecinae									
41	Scrobe below/ laterad compound eye	0	0	0	0	0	1	1	1
42	Scapes thickened distally, medial (apparent dorsal) articulatory ridge enlarged and elongated	0	0	0	0	0/1	1	1	1
43	Postgenal bridge less than half of head length (corresponds to length of mandibular abductor/ opener muscle 0md3 origin in *Tatuidris*)	0	0	0	0	0/1	1	?	1
44	Abdominal segment III strongly petiolated (see Figs. 13, 16, 17)	0	0	0	0	0	1	1	1

[5]. This new polarity hypothesis with respect to petiolar tergosternal fusion is dependent on the topologies of the Poneria and clades therein. The following observations may be made (see also Bolton 2003): The petiole is unfused in Ponerinae, where the laterotergites are usually present; the petiole is unfused and lacks laterotergites in many Amblyoponinae, although almost no amblyoponine has complete fusion (F. Esteves, pers. comm., draws attention to the complete fusion of *Onychomyrmex doddi*); it is unfused and possibly with laterotergites in *Apomyrma*; in contrast, it is without laterotergites in Paraponerinae, Proceratiinae, and Agroecomyrmecinae, and is completely fused in Paraponerinae and Agroecomyrmecinae, and partially fused in at least some *Proceratium* (Proceratiinae). The variability in Proceratiinae, including complete absence (or loss) of fusion in *Probolomyrmex*, raises the uncertainty of the proposed hypothesis. Notably, there is known variability in tergosternal fusion, as loss of this condition has also been observed for the abdominal segment IV in Amblyoponinae via *Adetomyrma* Ward, 1994 (e.g., Ward & Fisher 2016).

[6]. Species of the ponerine genus *Loboponera* have vaulted abdominal terga IV, for example, representing an instance of convergence with the Proceratiinae + Agroecomyrmecinae clade.

#	Definition	Po	Am	Ap	*Pa*	Pr	*An*	*Ag*	*Ta*
45–47: Apomorphies within Agroecomyrmecinae that depend on fossil placement									
45	Antennomere count reduced, less than 12 (see note 11 in †*Agroecomyrmex*)	0	0/1	0	0	0/1	0	1	1
46	Petiole extremely supraaxial and nearly vertically aligned, with posterior foramen raised high above anterior foramen (e.g., Boudinot 2015; it may be reversed in *Ankylomyrma*, whose condition is similar to that in some Amblyoponinae, but without a supraaxial helcium)	0	0	0	0	0	0	1	1
47	Postpetiole cylindrical and cheese-wheel-like, with sternum large and broadly convex	-	-	-	-	-	0	1	1
48–54: Possible synapomorphies of *Ankylomyrma*									
48	"Crown of thorns" flange developed along posterior head margin, anteriad occipital carina	0	0	0	0	0	1	0	0
49	Clypeus produced anteriorly as a lateromedially broad lobe	0/1	0	0	0	0	1	0	0
50	Postoccipital region encircled by dorsal and ventral occipital carinae	0/?	0	0	0	1?/?	1	?	0
51	Paired spines developed on mesonotum, propodeum, *and* petiole	0	0	0	0	0	1	0	0
52	Sternum of abdominal segment IV, when forming postpetiole, greatly reduced in size, being much shorter dorsoventrally than tergum	-	-	-	-	-	1	0	0
53	Abdominal tergum IV completely ovoid and with strong, laminar rim encircling terminal segments	0	0	0	0	0	1	0	0
54	Abdominal spiracle IV situated very distant from postpetiole (see Figs. 13, 16, 17)	0	0	0	0	0	1	?	0
55–92: Synapomorphies of *Tatuidris*									
55–60: Bite force optimized									
55	Head capsule broader than long (not accounting for lateral spines of *Ankylomyrma*)	0	0	0	0	0	0	0	1
56	Head posteriorly enlarged forming massive posterolateral lobes and posterior declivity dorsad postocciput	0	0	0	0	0	0	0	1
57	Mandibular adductor apodeme enlarged and sheet-shaped (see note 7)	0/?	?	?	?	?	?	?	1
58	Adductor muscle massively enlarged and only short tendon-fibrillae present (see note 7)	0/?	?	?	?	?	?	?	1
59	Anterior arms at right angle to long posterior arm, resulting in elevated position in head capsule (see note 7)	0/?	?	?	?	?	?	?	1
60	Resting position of head subprognathous (close to orthognathous) (*note*: due to postoccipital angle and position)	0	0	0	0	0/?	0	?	1
61–66: Mandibular articulation modified									
61	Mandibular acetabulum of cranium produced to apex of hypostoma (see note 8)	0	?	?	0	0	?	?	1

7. Internal anatomy and fine-scale morphology based on comparisons with *Brachyponera* (Richter & al. 2020).

8. Examination of the 3D models provided in Hita Garcia & al. 2019 (https://sketchfab.com/arilab/collections/discothyrea) suggests that the fimbrial carina may form part of the gripping edge of the mandible in *Discothyrea*; this will be of high value to formally evaluate. Based on images from Keller's (2011) atlas, the fimbrial carina is neither elongate nor forming part of the gripping edge in *Proceratium* or *Probolomyrmex*.

#	Definition	Po	Am	Ap	*Pa*	Pr	*An*	*Ag*	*Ta*
62	Medial portion of clypeal condyle elongated, forming clypeal condylar rail (first part of pivot-slide mechanism)	0	?	?	0	0	0	?	1
63	Lateral portion of clypeal condyle shortened, clypeal condylar lobe incurved (first part of stop-lock mechanism)	0	?	?	0	0	0	?	1
64	Atala massively enlarged compared to mandibular stem size with consequent broadening and deepening of atalar acetabulum	0	0	0	0	0	0	0	1
65	Proximomedial lobate process (canthellar lobe) developed on mandibular stem (second part of pivot-slide mechanism)	0	?	?	0	0	?	?	1
66	Mandibular acetabulum medially divided by pyramidal process with medial portion forming deep fossa (second part of stop-lock mechanism)	0	?	?	0	0	0	?	1
67–72: Mandibular grip enhanced									
67	Blade of mandible robustly thickened and strongly arched, thus bowl-shaped	0	0	0	0	0	0	?	1
68	Masticatory margins aligned for their whole length, thus mandibles not overlapping	0	0	0	0	0	0	0	1
69	Masticatory teeth in form of numerous, even crenulations	0	0	0	0	0	0	0	1
70	Fimbrial carina elongate and forming primary contact margin for gripping (see note 9)	0	0	0	0	0/1	0	?	1
71	Chetae of first fimbrial field comb-like, sandwiching fimbrial carina ventrally with the masticatory margin	0	0	0	0	0/1	0	?	1
72	Robustly thickened, curving chaetae developed in a second fimbrial field	0	0	0	0	0	0	?	1
73, 74: Antennal mechanical protection enhanced									
73	Frontal region expanded such that antennal scrobe encompasses entire lateral head surface, and antennal toruli wideset from each other	0	0	0	0	0	0	0	1
74	Scrobe deepened and widened such that entire antenna capable of concealment, consequently antennal toruli upside-down and scape proximally bent	0	0	0	0	0	0	0	1
75–78: Maxillolabial complex mechanical protection enhanced									
75	Proximolateral labral processes enlarged (first part of lateral labromaxillary lock mechanism) (see note 9)	0/1	0/1	?	0	1	?	?	1
76	Distal stipital processes elongated (second part of lateral labromaxillary lock mechanism) (see note 10)	0/1	0/1	?	0	0	?	?	1
77	Labral distal notch both shallow and fitting into the premental furrow (see note 11)	0/1	0/1	0	0	0	?	?	1

[9]. The specimen of *Proceratium pergandei* imaged in Keller's (2011) SEM atlas (ANTWEB1008584) has a disarticulated labrum. The lateral processes are as large as those of *Tatuidris tatusia*. We were unable to evaluate the labra of other proceratiines.

[10]. The specimens of *Discothyrea oculata* (ANTWEB1008518), *Proceratium pergandei* (ANTWEB1008584), and *Probolomyrmex guineensis* (ANTWEB1008582) in Keller's (2011) SEM atlas appear to have elongate distal maxillary processes; they are of a distinct shape relative to *Tatuidris*, and thus are scored 0 here.

[11]. The distal labral notch of the proceratiines imaged in Keller's (2011) SEM atlas may be shallow, but all of them have labra that overlap the prementum, rather than fitting into the premental groove, thus this lock mechanism is not formed.

#	Definition	Po	Am	Ap	*Pa*	Pr	*An*	*Ag*	*Ta*
78	Transverse premental furrow/groove clearly developed (part of the labrolabial lock mechanism) (see notes 12, 13)	0/1	0/1	0	1	0	1	?	1
79–92: Other apomorphies									
79	Cuticle highly polished in appearance (also, thick)	0/1	0/1	0	0	0	0	0	1
80	Clypeal furrow developed as deep groove	0	0	0	0	0	0	?	1
81	Anterior margin of clypeal lobe laminar	0	0	0	0	0	0	0	1
82	Antennomere count further reduced (see note 14)	0	0/1	0	0	0/1	0	0	1
83	Scape clavate (presumably flagellar muscles strengthened)	0	0	1	0	0/1	0	0	1
84	Antennomere proportions and sensilla armament of a complex form with enlarged apical antennomere with a group of sensilla placodea ventrally	0/1	?	0/?	0/?	0/1	0/?	0/?	1
85	Palpomere count reduced (1,2 or 0,2?) (see note 15)	0/1	0	0	0	0/1	0	?	1
86	Dorsal tentorial arm elongated, longer than 2/5 of anterior arm	0/?	?	?	?	?	?	?	1
87	Ventral thoracic contact surface of head widened (i.e., ventral occipital carina shifted orad)	0/?	0/?	0	0	0	0	?	1
88	Secondary ventromedial postoccipital process (subforaminal process) developed (see note 16)	0/?	?	?	0	1?	?	?	1
89	Posterior delimitation of clypeus weakly developed; supraclypeal area indistinct	0	0	1	0	0	0	0	1
90	Compound eyes reduced	0/1	1	1	0	0/1	0	0	1
91	Protibia with conspicuous apical seta brush on anterior/dorsal surface	0	0	0	0	0	0	0	1
92	Mesometapleural suture obliterated (= not sulcate) ventrad metathoracic (posterior) spiracle	0/1	0/1	1	0	0/1	0	?	1

[12]. The transverse premental furrow is absent in a narrow majority of the ponerine specimens imaged in Keller's (2011) atlas. The furrow is absent, indistinctly developed, or otherwise modified beyond direct recognition in the following: *Platythyrea*, *Ponera*, *Cryptopone*, *Dinoponera*, *Neoponera apicalis* (but present in *Neoponera villosa*), *Belonopelta*, *Harpegnathos*, *Brachyponera*, *Centromyrmex*, *Dolioponera*, *Hagensia*, *Ophthalmopone*, *Paltothyreus*, *Phrynoponera*, *Streblognathus*, *Leptogenys* (variable), *Anochetus*, and *Odontomachus*. All taxa from the atlas that are not listed here have a distinct furrow, with the exception of *Emeryopone*, for which the imaged specimen has had the maxillolabial complex dissected out.

[13]. From Keller's (2011) atlas, the proximal prementum of *Discothyrea testacea* (ANTWEB1008519), *Proceratium pergandei*, and *Probolomyrmex guineensis* can be seen to be longer than that of *Tatuidris*.

[14]. See also Hita Garcia & al. (2019) for anatomical details about antennomere count reduction in *Discothyrea*.

[15]. Scoring for Amblyoponinae based on Bolton (2003).

[16]. The specimen UFV-LABECOL-000032 of *Discothyrea bobi*, dissected and imaged by Júlio Chaul (Univ. Federal do Viçosa), appears to have this proximomedial process of the postocciput.

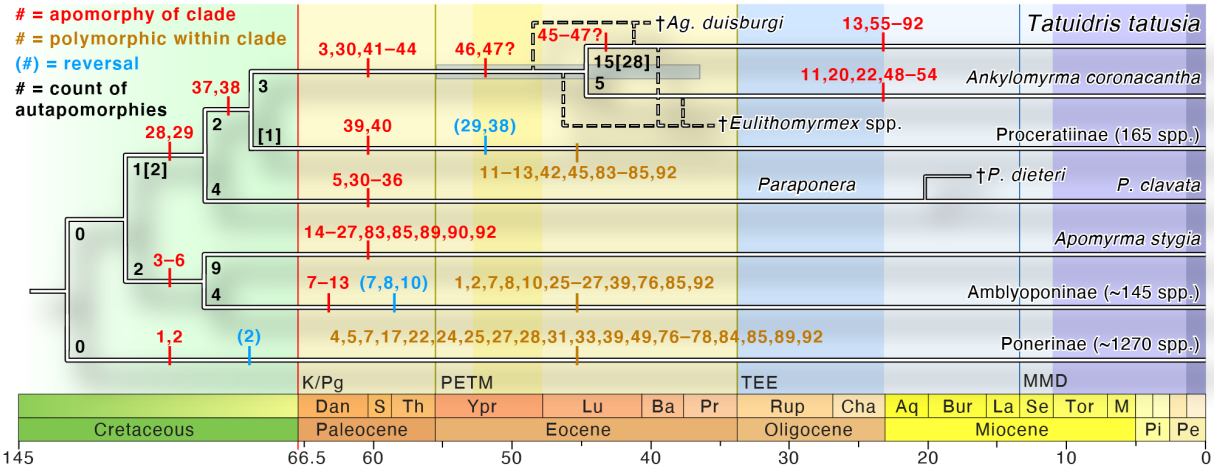

Fig. 12: Summary chronogram adapted from Borowiec & al. (2019) and Romiguier & al. (2022) displaying relationships, age estimates, and potential morphological transformation series within Poneria. Numbers: red = reasonable apomorphies; ochre = traits that are polymorphic across the given clade; blue = reasonable reversals; black = count of autapomorphies. Ambiguous apomorphies in terms of total autapomorphy count indicated by square brackets []. *Tatuidris tatusia* has 15 unambiguous and 13 ambiguous autapomorphies (i.e., which could not be evaluated across multiple terminals due to sampling limitations, chars 57 - 59, 61 - 63, 65, 66, 75, 76, 84, 86, 88 of Tab. 2), while three reasonable apomorphies are shared between †*Agroecomyrmex* and *Tatuidris*. The blue bar on the Agroecomyrmecinae node is the 95% highest probability densities for the age of the node from Borowiec & al. (2019). Colored boxes in the background correspond to major changes in global temperature based on the data of Zachos & al. (2001): light yellow = hot Earth; dark yellow = Eocene optimum; first blue = Oligocene cool Earth; second blue = early Miocene warm period; third blue = late Miocene cold period; fourth blue = Pliocene to Pleistocene colder period. Major or otherwise notable extinction events are indicated by vertical bars: K / Pg = end-Cretaceous crisis; PETM = Paleocene-Eocene thermal maximum; TEE = terminal Eocene event; MMD = mid Miocene disruption. See Table 2 for numbered morphological transformations. Note that the locations of the tick marks on the chronogram are not intended to indicate the exact geological time when the transformations occurred.

"pinching" of the frontal carinae and "fusion" of the medial torular arch and frontal carina – the former is reversed in *Platythyrea*, and the latter is homoplastic with respect to some Amblyoponinae. There are definitely complex patterns of variation within Ponerini (e.g., Schmidt & Shattuck 2014), but these derivations are not tabulated here as Ponerinae are not a focus of our study. Extensive study of Ponerinae, particularly the highly derived lineages, is desirable for future study.

For the newly recovered "PPA" clade (Paraponerinae + Proceratiinae + Agroecomyrmecinae) and "PA" clade (Proceratiinae + Agroecomyrmecinae) (Romiguier & al. 2022), we recognize two synapomorphies each plus a new synapomorphy for Proceratiinae. In contrast to other Poneria, the promesonotal articulation is fused in the PPA clade, with the dorsal suture retained in *Paraponera* and obliteration of this suture in the PA clade as a synapomorphic condition. The PPA clade may also be defined by complete tergosternal fusion of the petiole, although there is variability as the fusion is absent or incomplete in several Proceratiinae. The PA clade has a strongly vaulted abdominal segment IV. Vaulting and the fusions of the promesonotum and petiole have been recorded in prior studies (e.g., Bolton 2003, Keller 2011), but their polarities were not possible to reason out previously due to topological uncertainty. Finally, whereas Agroecomyrmecinae and *Discothyrea* retain a fine, external marking of the ventral (lateral) promesonotal suture, in other Proceratiinae, this marking is reduced (*Proceratium*) to completely obliterated (*Probolomyrmex*), completing a trend of mesosomal fusion.

Discussion

Overview

Among all ants, *Tatuidris tatusia* is one of the most alien in appearance, being lumbering, tank-like predators, with a highly compact mesosoma, strongly arched gaster, long sting, and a powerful, massive head that bears deep antennal scrobes. The head is "oversized" in comparison with other ants, approaching or exceeding the individual volumes of the mesosoma and metasoma. Like the mesosoma and the "waist", the cuticle of the cranium and mandibles is thick and strongly sclerotized, likely providing substantial mechanical protection as well as structural integrity. We hypothesize that the specific head architecture of *T. tatusia* results in high biting strength, mechanical protection, and balance via significant expansion of the frontal area in all directions, which also results in the highly unusual "shield-like" cranial form. We group these and other modifications that we record for the head of *T. tatusia* into six sets of structural characters of the head skeleton and the head appendages based on their presumed mechanical consequences (mechanical

Fig. 13: Summary of morphological characters of Agroecomyrmecinae, based on photographs of point-mounted specimens and an amber fossil from AntWeb (2022). **A, B:** *Tatuidris tatusia*. **C, D:** *Ankylomyrma coronacantha*. **E, F:** †*Agroecomyrmex duisburgi*. **A, C, E:** Full face view of the head. **B, D, F:** Lateral view of whole body, oblique in F. **B':** Detail of the petiole and postpetiole of *T. tatusia*. Characters are marked by number, corresponding to Table 2. Image credits: *T. tatusia* CASENT0423526 (A, B), CASENT0178755 (B'), and *Ankylomyrma coronacantha* CASENT0005904 by April Nobile; † *Agroecomyrmex duisburgi* BMNHP18831 by Vincent Perrichot.

"faculty" but not "biological role"; Bock & von Wahlert 1965). The modifications of these structural sets appear to be broadly related to: (1) mandibular closing kinematics (the mandible adductor / closer muscle 0md1, the forehead, and posterolateral bulges); (2) mandibular opening kinematics (the mandibular abductor / opener muscle 0md3, the postgenal box); (3) head orientation / balance (the cervical articulation, that is, the postocciput and its surrounding cuticular surfaces); (4) mouthpart interlocking (the oral foramen, that is, the clypeus and mouthpart articulation surfaces); (5) antennal kinematics / protection (the antenna, the antennal scrobe, and torular apparatus);

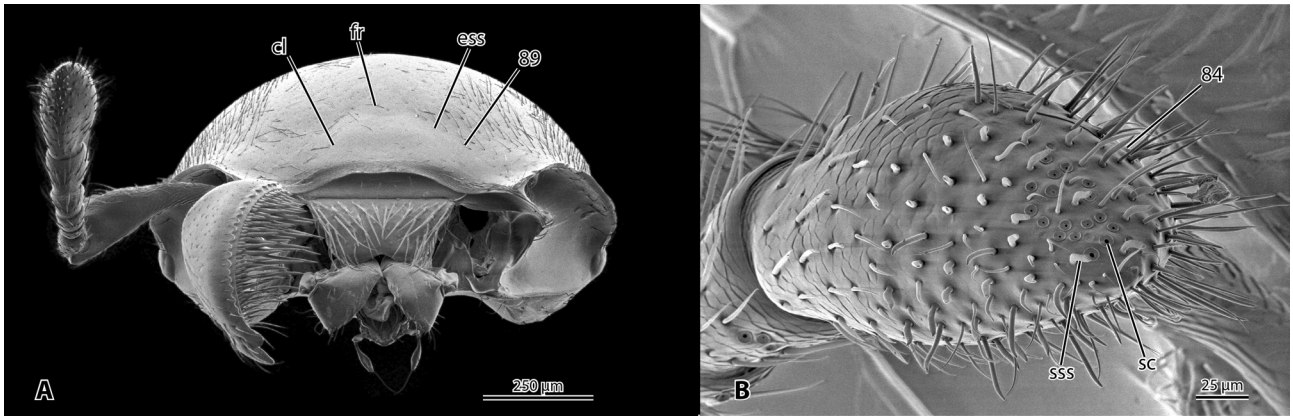

Fig. 14: Summary of morphological characters of Agroecomyrmecinae, based on scanning electron micrographs of a dissected specimen of *Tatuidris tatusia*, based on the morphological atlas of Keller (2011), accessed from AntWeb (2022). **A:** Head in frontal view. **B:** Ventral view of apical antennomere, showing sensilla. **Abbreviations: cl** – clypeus; **ess** – epistomal sulcus; **fr** – frontal area; **sc** – sensillum coeloconicum; **sss** – sickle shaped sensillum. Characters are marked by character number detailed in Table 2. Image credits: ANTWEB1008593 by Roberto Keller.

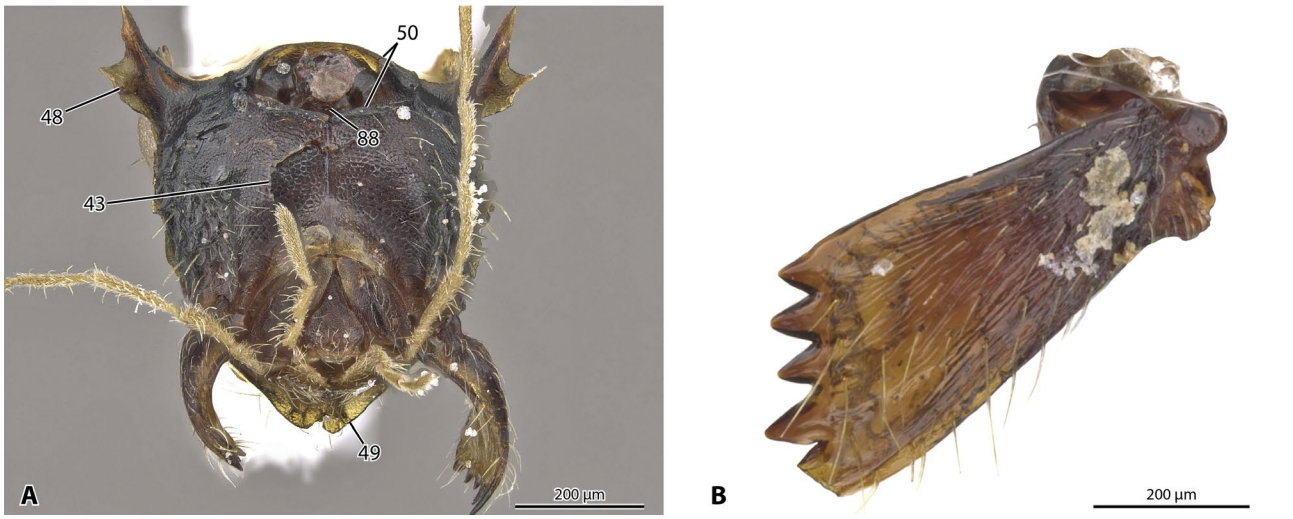

Fig. 15: Summary of morphological characters of Agroecomyrmecinae, based on photographs of a point-mounted, dissected specimen of *Ankylomyrma coronacantha*, from AntWeb (2022). **A:** Head in ventral view. **B:** Mandible in outer view. Characters are marked by number, corresponding to Table 2. Image credits: CASENT0005904 (A) by Estella Ortega, CASENT0902015 (B) by Will Ericson.

and (6) spatial organization in the head (the tentorium bearing muscular origins for the antenna and maxillolabial complex). We propose these sets for biomechanical / physiological studies in concert with ecological studies to better understand in how far the structural modifications of *T. tatusia* are "adaptations" to their ecology and lifestyle. For this contribution, we hypothesize potential biological roles of the modifications found in *T. tatusia* from an anatomical-functional perspective based on the limited knowledge available. Additionally, we assess the functional morphology of the mandible, we compare the pharyngeal apparatus with that of previously studied species, and we provide special considerations on the evolution of *T. tatusia* in the context of the Poneria and relative to other highly specialized and depauperate ant lineages. Note that the sets named above are only partly congruent with those used to organize characters in Table 2. The latter are convenient groupings to organize our entire character list, partly based on potential functions, the former are more specific structural modifications with possible mechanical consequences that we want to discuss here in more detail.

Hypothesized adaptations relating to aggression, defense, and balance

The visually most striking modifications of the *Tatuidris tatusia* head, compared with species retaining more plesiomorphies of the ant ground plan (e.g., Richter & al. 2022), are the shortening and broadening of the cranium, the lateral and posterior expansion of the frontal cephalic surface, and arguably thickening of the cuticle. We propose that all of these simultaneously enhance power (through

Fig. 16: Summary of morphological characters of Paraponerinae and Proceratiinae, based on photographs of point-mounted specimens from AntWeb (2022). **A, B:** *Paraponera clavata*. **C, D:** *Proceratium creek*. **E, F:** *Probolomyrmex guineensis*. **A, C, E:** View of the head, full face. **B, D, F:** Lateral view of whole body. Characters are marked by number, corresponding to Table 2. Image credits: *Paraponera clavata* CASENT0006789 and *Proceratium creek* CASENT0104439 by April Nobile, *Probolomyrmex guineensis* CASENT0249253 by Shannon Hartman.

mandibular muscles, see, e.g., Gronenberg & al. 1997), protection, and balance.

The shortening of the head is evinced by the relative length of the postgenal bridge (set 2), which is ~42% of the total head length in *Tatuidris tatusia*. This relative length is similar to that observed in stem ants (such as †*Gerontoformica* Nel & Perrault, 2004) and prognathous Aculeata (such as *Methocha* Latreille, 1804 and *Ampulex* Jurine, 1807) but is distinctly shorter than occurs in many other crown Formicidae (see Richter & al. 2022). A potential limit to this shortening is the length of the area of origin of the mandibular abductor / opener muscle (0md3), which extends across the entire postgenal ridge surface in *T. tatusia* (Fig. 4A, B); a case not yet observed

Fig. 17: Summary of morphological characters of Ponerinae, Amblyoponinae, and Apomyrminae, based on photographs of point-mounted specimens from AntWeb (2022). **A, B:** *Platythyrea lamellosa*. **C, D:** *Fulakora* bath5. **E, F:** *Apomyrma stygia*. **A, C, E:** View of the head, full face. **B, D, F:** Lateral view of the whole body. Characters are marked by number, corresponding to Table 2. Image credits: *Platythyrea lamellosa* CASENT0252018 by Bradley Reynolds, *F.* bath5 QMT152681 by Erin Prado, and *A. stygia* CASENT0000077 by April Nobile.

in other ants (Richter & al. 2019, 2020, Boudinot & al. 2021, Richter & al. 2021a, 2022). The expansion of the frontal surface correlates with two other modifications: the shift of the antennal scrobes to the lateral sides of the head (set 5) and the presence of the massive, muscle-filled posterolateral bulges that extend onto the ventral side of the head (Fig. 1C, set 1), resulting in the posterodorsal cranial declivity around and above the postoccipital complex (set 3). The posterolateral bulges also minimize the exposure of the cervical region, another potential defensive benefit.

In addition to these modifications, the cuticle is relatively thick, especially in the dorsal and lateral regions of the head – likely improving mechanical protection and integrity – and the mandibular adductor muscles are enormously enlarged. A relatively thick cuticle was also recorded for other Poneria, especially members of the closely related Proceratiinea (Peeters et al. 2017), but

ecological and phylogenetic patterns are not understood in detail at the moment. Although we do not have quantitative (i.e., volumetric) data for the entire body, it is apparent that the head of *Tatuidris tatusia* is massive compared with the mesosoma (Fig. 1). Thus, it is worth considering how the head balances. Similar to other large-headed ants (such as *Acanthomyrmex* Emery, 1893 and *Pheidole* Westwood, 1839 soldiers; see Moffett 1986, Wilson 2003), we observe that the postocciput is situated close to the mouth due to the short postgenal bridge, thus lying well beneath the mass of the posterior and posterolateral cranial elongations.

Modifications of the antennal apparatus and tentorium

Due to the lateral expansion of the frontal area of the head, the frontal lobes broadly overhang the wide and deep antennal scrobes dorsally, and the antennal articulations are oriented nearly upside-down, that is, facing the underside of the head rather than the dorsal / facial direction. The completely inverted antennal socket is likely unique among ants (Keller 2011). However, other ant species with wide frontal lobes may also approach this condition (e.g., *Phalacromyrmex* Kempf, 1960; see Bolton 2003 and Donoso 2012). A nearly complete inversion was also recently observed in a pselaphine beetle (Beutel & al. 2021). Together with the deep antennal scrobe that provides coverage for almost the entire antenna and the clavate scapus, this configuration results in a high degree of protection for the antennae of *Tatuidris tatusia*, although it likely also restricts antennal movement. This restriction is especially emphasized by the large torular lobe, which mechanically "forces" the antenna to rest inside the scrobe when it is retracted (Fig. 3C).

Corresponding to the far anterolateral position and inverted orientation of the antennal socket, a suite of tentorial modifications occurs (set 6). The attachment area for the extrinsic antennal muscles faces almost directly toward the antennal socket due to the shape of the anterior arm and, notably, the twist of its medial lamella (Fig. 3A, B). This condition presumably results in optimized use of the available space for muscle attachment and is likely necessary to reach the upward-facing rim of the bulbus. If the antennal muscles originated further ventrally relative to the antennal socket, as in other ants (e.g., Kubota & al. 2019, Richter & al. 2019, 2020), their tendons would have to curve downward to reach the bulbus, which might be mechanically unfavorable. A considerable portion of Musculus tentorioscapalis lateralis (0an3) originates on the dorsal tentorial arm. As this shifts its origin further dorsad compared with other ants studied so far (Richter & al. 2019, 2020, 2021a), this can likely be seen in the same functional context. In *Tatuidris tatusia*, this antennal muscle configuration is also supported by elongation and a 90° bend of the posterior tentorial arms, which result in an overall elevated position of the tentorium in the lumen of the head. This may also allow for maximal use of space by the mandibular adductor muscles.

Some of these modifications are an interesting parallel to the condition in *Protanilla lini* Terayama, 2009, where the zigzag-shaped anterior arms and the twist of the medial lamellae presumably also optimize the attachment area for the extrinsic antennal muscles to the almost anteriorly directed antennal socket. Richter & al. (2021a) hypothesized that the origin of 0an3 on the dorsal tentorial arm could be a plesiomorphic condition retained in Leptanillomorpha. Even though this may be the case, the observations made in the present study suggest that such a condition could have evolved (or re-evolved) several times in Formicidae and other groups of Aculeata (Richter & al. 2022), indicating that this is a highly variable condition possibly linked with specific functional or spatial constraints.

Mandibular form and function

The mandibles, the mandibular articulations, and the adductor muscles of *Tatuidris tatusia* are modified in a way that may enhance the physical capacities for power exertion, energy transfer, and grip (see section "Possible mandibular motions" above, and Fig. 12, Tab. 2). The mandibles are massive, with a bowl-shaped blade that bears a dense brush of chaetae subtending two rims; one is crenulate and corresponds to the "masticatory margin" of other ants, the other is sharp, straight, and corresponds to the fimbrial line carina (Fig. 4). The shape of the blade is nearly unique among ants, with parallels only observed in the myrmicines *Ishakidris* Bolton, 1984 and *Phalacromyrmex* (see Kempf 1960, Bolton 1984, 1998, Donoso 2012) and stem ants of the †*Camelomecia* Barden & Grimaldi, 2016 genus group (Boudinot & al. 2020). Similar chaetal brushes, however, have also been observed in †*Zigrasimecia* Barden & Grimaldi, 2013 (Cao & al. 2020) and the extant genera *Protanilla* Taylor, 1990 (Richter & al. 2021a) and to a lesser extent *Discothyrea* Roger, 1863 (Hita-Garcia & al. 2019). The fact that reduction of the mandibular teeth in these lineages correlates with the development of chaetal brushes suggests a possible functional tradeoff between friction- and incisor-based grip.

Although the taxonomic sampling of published depictions (e.g., based on µ-CT-scans) of ant mandibular bases is still limited, it is apparent that the mandibular articulations of *Tatuidris tatusia* are highly derived within the family (set 4). Both the ventral (primary) and dorsal (secondary) mandibular articulations differ strikingly from the corresponding joints in other ant species (Richter & al. 2019, 2020, Boudinot & al. 2022a). These unique conditions coincide and possibly correlate with the general modification of the clypeus and its anterior and lateral projections above the mandible. Due to this configuration, the cephalic condyle is not on the anterolateral corner of the clypeus, as in most other ants, but on the ventral surface of the clypeal projection. Additionally, the condyle is L-shaped and divided into two distinctive parts (Fig. 2D): the condylar lobe, a short dorsoventral projection corresponding more or less with the condyle of other ants, and the condylar rail, a transverse ridge

(long part of the "L") that is either a modification of a part of the condyle or a modification of the triangular clypeal projection, observed, for example, in *Wasmannia* Forel, 1893 (Richter & al. 2019). Consequently, the articulatory surface of the mandible is unusually complex (Fig. 4C). The mandibular acetabulum is divided into a medial and a lateral groove by a short ridge. The condylar lobe interacts with these two grooves, while the condylar rail interacts with the distal contact surface and the medial groove, areas of the mandibular stem unmodified in many other ants (Richter & al. 2019, 2020, Boudinot & al. 2022a). Additional notable modifications of the mandible are the shift of the primary mandibular condyle medially in its broad articulatory fossa of the cranium and the thickening and rotation of the canthellus, forming the canthellar groove interacting with the triangular hypostomal process.

Based on these structural modifications, we have presented our hypothesized movement pattern for the mandible in the results section. This adds to the known mechanical diversity of mandible opening / closing in ants, so far described for trap-jaw ants (e.g., Gronenberg 1995, Larabee & al. 2017, Booher & al. 2021), *Protanilla lini* (see Richter & al. 2021a), and *Harpegnathos* Jerdon, 1851 (Zhang & al. 2020). If 3D-printed models are more precisely constructed in the future and potentially include soft parts of the articulation, they may be used to conduct actual kinematic analyses to better understand the range of mandibular motion. One exciting application would be modeling mandibular motions of extinct species such as †*Camelomecia janovitzi* Barden & Grimaldi, 2016 (see also Boudinot & al. 2020), which has mandibles that are exceptionally similar in shape to those of *Tatuidris tatusia*.

In the context of mandibular functional morphology, it is also important to address the anatomy of the adductor muscle (0md1). This muscle is massive, filling out almost the entire lateral space within the head capsule in *Tatuidris tatusia* (Fig. 4A). Additional space for this muscle is provided not only by the broad and posteriorly expanded head capsule but also by the ventral lateral bulges and the bent tentoria. Further, most of the muscle fibers in the head likely are fast-contracting fibers (Fig. 5A). As revealed by Gronenberg & al. (1997), the fibers in the adductor muscle of ants can have either long or short sarcomeres, specialized for either powerful or fast contractions, respectively. Long-sarcomere fibers come in two further configurations: They are either directly attached to the main apodeme of the muscle or connect to it via thin cuticular threads. Our µ-CT data were insufficient to assess sarcomere length accurately, and our histological sections were not optimized (e.g., in orientation) for sarcomere-length measurements. However, we observed that those fibers attached to the central region of the massive apodeme lack threads. Our histological data corroborate a short sarcomere condition for these fibers. Only the fibers attached to the edges of the apodeme have both threads and long sarcomeres.

The apodeme is expanded as a large, flat sheet of cuticle and provides sufficient attachment space for the many directly attaching fibers. The high proportion of short sarcomere fibers and the muscle size likely produce a relatively fast yet powerful bite of the mandible (see also Püffel & al. 2021 for a discussion of functional consequences of mandibular muscle architecture). *Tatuidris tatusia*, thus, have morphological characteristics that enable them to employ the "static" method of prey control (Bolton 1998), that is, remaining clamped on the prey until the sting is used. Another remarkable aspect concerning the unusual mandible of *T. tatusia* is the presence of the inner mandibular gland, opening with a sieve plate at its lateral base. A gland of this specific configuration has not been found in any other ant species so far (Billen & Delsinne 2014). The function of the gland is currently unknown, but it may be functionally related to the peculiar mandibular form and movement.

While the prey of *Tatuidris tatusia* remains unknown (Jacquemin & al. 2014), it is conceivable that *T. tatusia* rely on their chaetal comb to grip small, round arthropods, such as Oribatida or other Acari. However, the proportion of fast-contracting fibers combined with the friction-supporting mandibular brush could conceivably also allow *T. tatusia* to catch fast prey such as Collembola. We agree with Jacquemin & al. (2014) that the overall slow movements, highly defensive external morphology, and reduced eyes suggest that *T. tatusia* may be slow ambush predators of the leaf litter or upper soil layers rather than active hunters. Previously, it was proposed that some species in the genus *Strumigenys* Smith, F., 1860 use chemical lures to attract prey (Dejean 1985). If *T. tatusia* indeed were an ambush predator, its intramandibular gland may serve such a function. More observational and experimental work is needed.

Comparative anatomy of the pharyngeal apparatus

As the pharyngeal apparatus is a source of phylogenetic information that has only recently been tapped into, we dedicate a brief comparative discussion to this subject. The anterior prepharynx of *Tatuidris tatusia* is similar to that of *Protanilla lini* (see Richter & al. 2021a) and *Brachyponera* Emery, 1900 (Richter & al. 2020) in its overall shape and pattern of sclerotization, suggesting that this may represent a plesiomorphic configuration in crown Formicidae. As in *P. lini*, the upward curving posterior parts of the oral arms form a broad concave wall. As in *Brachyponera*, the dorsal plates are high and elongated. Both features are also similar in male *Dorylus helvolus* (Linnaeus, 1764) (see Boudinot & al. 2021) but not *Wasmannia affinis* Santschi, 1929 (Richter & al. 2019) or *Formica rufa* Linnaeus, 1761 (Richter & al. 2020). The ventral prepharyngeal dilatator has anterior and posterior insertion areas that are distinctly separated; this supports the previous interpretation that this muscle might consist of both 0bu5 and 0bu6 (Richter & al. 2019, 2020). The long tentorio-oral muscle 0hy2 resembles the condition in *Protanilla* (see Richter & al. 2021a). However, this is most likely a result of convergent / parallel

evolution caused by the anterior shift of the antennal socket relative to the anatomical mouth opening in both species. The shape of the pharyngeal gland is similar to that described in *Brachyponera* (see Richter & al. 2020) and several other representatives of Poneria (Schoeters & Billen 1996), supporting the notion that this condition may be a synapomorphy of the whole clade.

Evolutionary implications: derived conditions of the Agroecomyrmecinae

At the given scale of comparison (Fig. 12, Tab. 2), *Tatuidris tatusia* is the taxon with the most derived conditions in our present assessment of morphological evolution in Poneria, followed by the exceptional and monotypic lineage Apomyrminae (*Apomyrma stygia*). Various aspects of the exceptional morphology of *T. tatusia* are paralleled in the fossil record in lineages such as †*Zigrasimecia* and †*Camelomecia janovitzi*, which raises a number of questions. What is the timescale of extreme derivation, and what are the selection forces that drive the evolution of these forms? What do these ants do in nature, and can *T. tatusia* shed light on the paleoecology of Mesozoic Formicoidea? In overall cephalic and mesosomal form, the big-headed and tank-like *T. tatusia* is superficially but still remarkably similar to †*Zigrasimecia* (Cao & al. 2020; see also Boudinot & al. 2022b). In the unusual and specific form of the mandibular tool edge, *T. tatusia* and †*C. janovitzi* are nearly identical. While there is far too little known about the behavioral ecology of *T. tatusia* and these Mesozoic ants to address potential behavioral similarities, the phylogenetic relationships of the Agroecomyrmecinae may provide some insight into the timescale and selective context driving their phenotypic evolution. Table 2 and Figures 12 - 17 provide an overview of our favored phylogenetic topology and a series of potential morphological transformations in Agroecomyrmecinae and related subfamilies based on our present study, for which the implicit ground plan hypothesis was informed by the ancestral state analyses of Boudinot & al. (2022a) and Richter & al. (2022).

As outlined in the Introduction, the extant sister group of *Tatuidris tatusia* is known to be *Ankylomyrma* Bolton, 1973 (Ward & al. 2015), the two comprising the extant members of the subfamily Agroecomyrmecinae. This clade has been variably supported as sister to the "bullet ant", *Paraponera* Smith, F., 1858 (Brady & al. 2006, Moreau & al. 2006, Branstetter & al. 2017, Borowiec & al. 2019), with a recent phylogenomic study more strongly supporting a sister-group relationship to Proceratiinae (Romiguier & al. 2022). The relationships of the two fossil genera †*Agroecomyrmex* (Baltic amber) and †*Eulithomyrmex* (Florissant shale) are far less certain, although †*Agroecomyrmex* and *T. tatusia* do clearly share a series of derived conditions (Figs. 12 and 13, Tab. 2; Wheeler 1915).

Previous molecular phylogenetic analyses supporting Paraponerinae and Agroecomyrmecinae were criticized by being unexpected based on morphology alone (e.g., Baroni Urbani & de Andrade 2007); we observe that, with the topology of Romiguier & al. (2022), it is possible to reason out character polarity hypotheses for promesonotal fusion of the mesosoma and, to some degree, the tergosternal fusion of the petiole. The remarkable development of antennal scrobes that can contain the entire scape would be a potential synapomorphy of Agroecomyrmecinae + Paraponerinae. However, considering the different position of the scrobe relative to the eye, the Proceratiinae + Agroecomyrmecinae relationship indicates that this may be parallelism. The vaulting of abdominal tergum IV in Proceratiinae and Agroecomyrmecinae, however, becomes a reasonable synapomorphy as well as the obliteration of the dorsal portion of the promesonotal suture, which is retained in *Paraponera*. Based on the divergence dating estimates of Borowiec & al. (2019) and Romiguier & al. (2022), the crown ages of the Poneria, Ponerinae, Amblyoponinae, and Proceratiinae are Cretaceous. While the crown ages of Agroecomyrmecinae and Paraponerinae are almost certainly Cenozoic, the ancestor of Agroecomyrmecinae + Proceratiinae likely displayed a compact mesosoma with promesonotal fusion prior to the end-Cretaceous turnover event. By or perhaps after the Paleocene-Eocene thermal maximum, the ancestor of the Agroecomyrmecinae may have derived posteriorly shifted compound eyes, well-developed frontal lobes, and robust scapes, among other features (Figs. 12, 13). Comparison of †*Agroecomyrmex duisburgi* and *Ankylomyrma* with *Tatuidris tatusia* using µ-CT data will certainly enrich our knowledge of the history of this group.

Despite the derivation of the "crown of thorns" cranial lamella, *Ankylomyrma coronacantha* has retained a head morphology characterized by more plesiomorphic features than *Tatuidris tatusia*. Some of these relative plesiomorphies include the flat mandible with five teeth (Fig. 15B; resembling the weakly torqued planar form as defined by Keller 2011), the absence of the chaetal field, the less expanded frontal region / frontal lobes, absence of the posteroventral cephalic lobes, the 12-merous antennae, the relatively large compound eyes (although eye size is generally variable and polarity uncertain), and a more open configuration of the mouthparts (Fig. 15A). Specifically, the hypostoma of *Ankylomyrma* is much more open in ventral view. Moreover, the maxillary and labial palps are significantly longer with more palpomeres that are also individually longer; however, the elongation may be a secondary derivation of *Ankylomyrma* compared to the short palpomeres of relatives such as *Paraponera* and Proceratiinae.

While *Ankylomyrma* shows more plesiomorphic features relative to *Tatuidris tatusia*, many morphological characteristics of this genus are likely specialized in their own right, considering the arboreal lifestyle of this species (Bolton 1973). Clear indications of this are the comparatively larger compound eyes and the protective spines. The ecological correlates of ant maxillolabial complex architecture are uncertain, and while the long palps of *Ankylomyrma* may intuitively be related to foraging in more open, for example, arboreal, habitats, there is no

clear evidence for such an association. In contrast, due to their shorter palpomeres and hypostomal configuration, *T. tatusia* may seal the oral foramen more tightly, which intuitively would lead to improved protection in cryptic habitats or from potentially defensive prey. However, the functional context of tight mouthpart closure is similarly poorly known as that of palpomere length.

Interestingly, the mandibular shape of *Ankylomyrma* could be associated with canopy living to a certain degree. It is similar to the "planar" mandibular form, which also occurs in the arboreal genus *Pseudomyrmex* Lund, 1831 (see Keller 2011), although the specific mandibular shape is different. A detailed study of the internal anatomy of *Ankylomyrma* may reveal additional cephalic synapomorphies with *T. tatusia* and will likely contribute to the further polarization of the character states of the armadillo ant (Fig. 12, Tab. 2).

Evolutionary implications: "relictual" lineages

We reiterate that, among examined representatives of Poneria, *Tatuidris tatusia*, *Ankylomyrma*, *Paraponera*, and *Apomyrma* represent morphologically disparate and phylogenetically isolated lineages for which relatively little morphological variation is known in the extant populations. Pie & Feitosa (2016) consider lineages characterized by phylogenetic isolation and a species-poor extant fauna as "relictual"; they indicate *T. tatusia* and *Paraponera* as typical representatives of such lineages. Based on their modeling, the survival of such lineages along evolutionary time is unlikely, so they propose two specific scenarios for their persistence: adaptation to a stable but specialized niche (hypothesis 1) or survival on insular landmasses with depauperate competition (hypothesis 2). Due to the widespread occurrence of *T. tatusia*, they recognized this genus as an example for the first hypothesis.

Considering the incomplete investigation of species diversity in *Tatuidris tatusia* and with the potential for some species to be delimited in the future (Donoso 2012; J. T. Longino, pers. comm.), the "relictuality" of this lineage from a diversity perspective will require additional scrutiny. Nevertheless, a > 40 million year old clade (Fig. 12), with a few species, may still fulfill the criterion of "disproportionately low species richness" given by Pie & Feitosa (2016). At this point it is important to note a critical distinction as the concept of "relictuality" has also been used to refer to paleogeographical relicts that retain an ancient geographical range relative to related lineages with a novel distribution, exemplified by the highly morphologically distinct *Leptomyrmex relictus* Boudinot & al. 2016 (see also Barden & al. 2017). In the following, we will focus our thoughts on the phylogenetic isolation concept of "relictual" lineages.

While not being a criterion for the definition of phylogenetic relictuality, we consider morphological stability or stasis to be an interesting aspect of understanding the evolution of "relictual" lineages: Should a phylogenetically isolated species (or species complex of a few similar species) be considered a paleomorphological "relict" if its derivations are extreme and relatively recent or at least not evinced in the fossil record? Among the four genera indicated at the beginning of this section, we observe that *Ankylomyrma* displays several symplesiomorphies of the head with †*Agroecomyrmex duisburgi* that have been stable since at least the Eocene (~40 million years (Ma)) and which are not shared with *Tatuidris tatusia* (Fig. 12, Tab. 2). Many of these same plesiomorphies are preserved in *Paraponera*; however, little can be said about the age of its defining synapomorphies except that this lineage has been stable since the mid Miocene (~15 Ma), as evinced by the high degree of similarity between †*P. dieteri* (see Baroni Urbani 1994) and *P. clavata*. Regardless, there is a spectrum of morphological derivation across these isolated lineages, with *Apomyrma* and *T. tatusia* at one extreme of the range (based on number of apomorphies). While the history of such character state transformations in geological time is elusive, fossils can be a way to trace them. Due to its position (Fig. 12), †*A. duisburgi* indicates that many of the autapomorphies of *T. tatusia* date to the Eocene. This further suggests a short timespan of morphological transformation and a possibly increased rate of modification relative to *Paraponera* and *Ankylomyrma*, despite the unusual morphology of the latter.

While we have made an effort to avoid bias in our character assessment, our coding scheme necessarily remains subjective; thus, the count of apomorphies is expected to change with a different approach to character coding and analysis (see section "Comparative morphology") and especially with additional data. Nevertheless, it seems obvious that *Tatuidris tatusia* is a species with an extreme accumulation of derived features; Figure 12 and Table 2 show that *T. tatusia* has, in our estimation, several times more apomorphies than *Ankylomyrma* and *Paraponera* and almost twice as many as *Apomyrma*. Moreover, the head of *T. tatusia* is characterized by a complex suite of interconnected modifications, based on our present assessment. The structural transformations of its head involve many characters that are not closely correlated in an obvious way according to our interpretation but instead belong to at least five different mechanical syndromes (Tab. 2). As a counterexample, the functionally and structurally modified head of species of the genus *Strumigenys*, defined by a trap jaw mechanism, evolved several times independently from non-trap-jaw relatives. Small but significant realignments of mouthpart structures lead to a switch-like reorganization of many head structures, which ultimately resulted in similar morphology in all lineages that have this mechanism, including specific modifications of musculature and the nervous system (Booher & al. 2021). In *T. tatusia*, the extreme derivation and total lack of morphologically intermediate lineages pose a conundrum: How does an extremely modified, phylogenetically isolated lineage come to be so, and what would this tell us about its "relictuality"?

We can only speculate about the exact evolutionary processes resulting in the wonderfully weird head morphology of *Tatuidris tatusia*. Did the many structural

derivations of the head assemble gradually over time, or is there a morphological switch, that is, a key change that triggered the large-scale reorganization of the head, similar to what occurs in *Strumigenys*? A candidate for such a switch may be the broadening of the frontal region and head in general, which directly leads to the rotated antennal socket and additional space for musculature and influences the mandibular articulation through the projection of the clypeus above the clypeal condylar area. However, the exact conformation of the mandibular articulation as well as the mandibular shape and chaetal brush are not necessarily logical outcomes of this change, indicating that there may have been intermediate states leading up to the extremely derived condition currently seen. That such morphological intermediates have apparently not survived to the present indicates that climatic events and vegetational turnovers may have played an important role in the evolution of the genus, with subsequent "runaway" derivation of the head and associated mechanisms, potentially as optimization of the functional traits discussed previously (predation, protection, and balance).

Certainly, *Ankylomyrma* and *Paraponera* also experienced similar turnover, but they accumulated much fewer morphological apomorphies (particularly of the head). Whether the derivation of the *Tatuidris tatusia* morph was a rapid burst (switch-like), long fuse (gradual), or jittery sprint (a combination of both), the armadillo ant represents a special case among its unusual relatives. Is their unique head a recent evolutionary event or are they paleomorphological relicts that retained this configuration for tens of millions of years? A detailed molecular investigation of the living population may help in at least establishing a minimum age for this question. Ultimately, future findings of *Tatuidris*-line fossils would provide a window into their evolutionary history and potential solution to the conundrum of "runaway relicts".

Conclusions

Our study of the head anatomy of *Tatuidris tatusia* builds on the recently established conceptual framework for the head morphology of Formicidae (Richter & al. 2019, 2020, 2021a, 2022, Boudinot & al. 2021). Through detailed documentation of the cephalic anatomy of *T. tatusia* and comparison with other ants, we reconstruct the complexity of modifications that have evolved in this lineage. These have resulted in a head morphology that appears to be optimized for prey capture (mandibular morphology and muscle architecture), protection (thick cuticle, antennal protection, tight maxillolabial complex closure), and balance (position of the occipital foramen, distribution of mass in the head). We find that the mandibular motion of *T. tatusia* is structurally constrained by their complex articulations, allowing us to precisely reason the mechanical function of opening and closing, which is unique among ants studied to date.

Benefitting from the phylogenetic resolution provided by DNA-sequence data – thus removing the confounding factor of relationship uncertainty to some degree – we propose a transformation series leading to the modern form of the *Tatuidris tatusia* head. Further, we recognize that *T. tatusia* is sui generis among Poneria, being an exceptionally modified "runaway relict". While more formal testing the evolutionary sequence leading to modern *T. tatusia* is outside of the scope of the present work, our considerations set up three major goals for the understanding of *T. tatusia* and other phylogenetically isolated and species-poor lineages, whether their morphology is dominated by relatively plesiomorphic or derived characters: (1) population-level phylogenomic analysis and reassessment of morphological variation (how old is the crown group; are there multiple sympatric species that have not been detected?), (2) analysis and exploration of the fossil record (evaluate the anatomy of †*Agroecomyrmex*, at the least), and (3) focused study on the natural history of these singular ants. Resolving these questions will contribute to our understanding of the patterns and processes of morphological macroevolution and may shed light on the evolutionary dynamics of the Formicoidea from their Mesozoic origin to their Cenozoic modernity. Interrogation of fossil and extant anatomy is a necessity.

Acknowledgments

We gratefully acknowledge the donation of several specimens of *Tatuidris tatusia* for µ-CT scanning by Jack Longino and by Thibaut Delsinne for histological examination. AR thanks Crystal Maier and Charles Whittemore Farnum for facilitating his stay at the Harvard Museum of Comparative Zoology and for databasing the specimen of *T. tatusia* examined there. We thank the Okinawa Institute of Science and Technology Graduate University (OIST) Imaging Section for providing access to the Zeiss Xradia µ-CT scanner and Shinya Komoto for general support. An Vandoren prepared the histological sections of *T. tatusia*, which we gratefully acknowledge. We are also very thankful to Michael Branstetter for providing us with pictures of living *T. tatusia*, which are valuable considering the rare collection of living specimens of this species. We thank Toni Wöhrl for taking the time to discuss the mandibular opening mechanism with us from a biomechanical perspective. We also thank the anonymous reviewers and Subject Editor Flávia Esteves for comments that improved the quality of the present study. AR gratefully acknowledges support by a scholarship and travel grant of the Evangelisches Studienwerk Villigst eV, which allowed him to visit the MCZ. BEB is supported by an Alexander von Humboldt Research Fellowship. FHG was supported by Japan Society for the Promotion of Science (JSPS) grants-in-aid KAKENHI grants (No. 18K14768 & 21K06326).

Conflict of interest

None.

Contributions of authors

Conceptualization: AR, BEB. Methodology: AR, BEB, FHG, JB. Investigation: AR, BEB. Resources: FHG, RGB,

JB, EPE. Data curation: AR, BEB, FHG. Writing, original draft: AR, BEB. Writing, review & editing: all authors. Visualization: AR, BEB. Supervision: RGB, EPE.

References

AntWeb 2022: AntWeb Version 8.68.7. California Academy of Science. – <https://www.antweb.org.>, retrieved on 25 January 2022.

Barden, P., Boudinot, B.E. & Lucky, A. 2017: Where fossils dare and males matter: combined morphological and molecular analysis untangles the evolutionary history of the spider ant genus *Leptomyrmex* Mayr (Hymenoptera: Dolichoderinae). – Invertebrate Systematics 31: 765-780.

Baroni Urbani, C. 1994: The identity of the Dominican *Paraponera* (Amber Collection Stuttgart: Hymenoptera, Formicidae. V: Ponerinae, partim). – Stuttgarter Beiträge zur Naturkunde. Serie B (Geologie und Paläontologie) 197: 1-9.

Baroni Urbani, C. & de Andrade, M. 1994: First description of fossil Dacetini ants with a critical analysis of the current classification of the tribe (Amber Collection Stuttgart: Hymenoptera, Formicidae. VI. Dacetini). – Stuttgarter Beiträge zur Naturkunde. Serie B (Geologie und Paläontologie) 198: 1-65.

Baroni Urbani, C. & de Andrade, M. 2007: The ant tribe Decetini: limits and constituent genera, with descriptions of new species. – Annali del Museo Civico di Storia Naturale "Giacomo Doria" 99: 1-191.

Baroni Urbani, C., Bolton, B. & Ward, P.S. 1992: The internal phylogeny of ants (Hymenoptera: Formicidae). – Systematic Entomology 17: 301-329.

Beutel, R.G., Luo, X.-Z., Yavorskaya, M.I. & Jałoszyński, P. 2021: Structural megadiversity in leaf litter predators – the head anatomy of *Pselaphus heisei* (Pselaphinae, Staphylinidae, Coleoptera). – Arthropod Systematics & Phylogeny 79: 443-463.

Billen, J. & Delsinne, T. 2014: A novel intramandibular gland in the ant *Tatuidris tatusia* (Hymenoptera: Formicidae). – Myrmecological News 19: 61-64.

Bock, W.J. & Von Wahlert, G. 1965: Adaptation and the form-function complex. – Evolution 19: 269-299.

Bolton, B. 1973: A remarkable new arboreal ant genus (Hym. Formicidae) from West Africa. – Entomologist's Monthly Magazine 108: 234-237.

Bolton, B. 1984: Diagnosis and relationships of the myrmicine ant genus *Ishakidris* gen. n. (Hymenoptera: Formicidae). – Systematic Entomology 9: 373-382.

Bolton, B. 1998: Monophyly of the dacetonine tribe-group and its component tribes (Hymenoptera: Formicidae). – Bulletin of the Natural History Museum Entomology Series 67: 65-78.

Bolton, B. 1999: Ant genera of the tribe Dacetonini (Hymenoptera: Formicidae). – Journal of Natural History 33: 1639-1698.

Bolton, B. 2000: The ant tribe Dacetini. – Memoirs of the American Entomological Institute 65: 1-1028.

Bolton, B. 2003: Synopsis and classification of Formicidae. – Memoirs of the American Entomological Institute 71: 1-370.

Booher, D.B., Gibson, J.C., Liu, C., Longino, J.T., Fisher, B.L., Janda, M., Narula, N., Toulkeridou, E., Mikheyev, A.S., Suarez, A.V. & Economo, E.P. 2021: Functional innovation promotes diversification of form in the evolution of an ultrafast trap-jaw mechanism in ants. – Public Library of Science Biology 19: art. e3001031.

Borowiec, M.L., Rabeling, C., Brady, S.G., Fisher, B.L., Schultz, T.R. & Ward, P.S. 2019: Compositional heterogeneity and outgroup choice influence the internal phylogeny of the ants. – Molecular Phylogenetics and Evolution 134: 111-121.

Boudinot, B.E. 2015: Contributions to the knowledge of Formicidae (Hymenoptera, Aculeata): a new diagnosis of the family, the first global male-based key to subfamilies, and a treatment of early branching lineages. – European Journal of Taxonomy: art. 120.

Boudinot, B.E., Khouri, Z., Richter, A., Griebenow, Z.H., van de Kamp, T., Perrichot, V. & Barden, P. 2022a: Evolution and systematics of the Aculeata and kin (Hymenoptera), with emphasis on the ants (Formicoidea: †@@@idae fam. nov., Formicidae). – bioRxiv; doi: 10.1101/2022.02.20.480183.

Boudinot, B.E., Moosdorf, O.T.D., Beutel, R.G. & Richter, A. 2021: Anatomy and evolution of the head of *Dorylus helvolus* (Formicidae: Dorylinae): patterns of sex- and caste-limited traits in the sausagefly and the driver ant. – Journal of Morphology 282: 1616-1658.

Boudinot, B.E., Perrichot, V. & Chaul, J.C.M. 2020: † *Camelosphecia* gen. nov., lost ant-wasp intermediates from the mid-Cretaceous (Hymenoptera, Formicoidea). – ZooKeys 1005: 21-55.

Boudinot, B.E., Probst, R.S., Brandão, C.R.F., Feitosa, R.M. & Ward, P.S. 2016: Out of the Neotropics: newly discovered relictual species sheds light on the biogeographical history of spider ants (*Leptomyrmex*, Dolichoderinae, Formicidae). – Systematic Entomology 41: 658-671.

Boudinot, B.E., Richter, A., Katzke, J., Chaul, J.C.M., Keller, R.A., Economo, E.P., Beutel, R.G. & Yamamoto, S. 2022b: Evidence for the evolution of eusociality in stem ants and a systematic revision of †*Gerontoformica* (Hymenoptera: Formicidae). – Zoological Journal of the Linnean Society 195: 1355-1389.

Brady, S.G., Schultz, T.R., Fisher, B.L. & Ward, P.S. 2006: Evaluating alternative hypotheses for the early evolution and diversification of ants. – Proceedings of the National Academy of Sciences of the United States of America 103: 18172-18177.

Branstetter, M.G. & Longino, J.T. 2022: UCE phylogenomics of New World *Cryptopone* (Hymenoptera: Formicidae) elucidates genus boundaries, species boundaries, and the vicariant history of a temperate-tropical disjunction. – Insect Systematics & Diversity 6: art. 6.

Branstetter, M.G., Longino, J.T., Ward, P.S. & Faircloth, B.C. 2017: Enriching the ant tree of life: enhanced UCE bait set for genome-scale phylogenetics of ants and other Hymenoptera. – Methods in Ecology and Evolution 8: 768-776.

Breed, M.D. & Harrison, J.M. 1985: Worker size, ovary development and division of labor in the giant tropical ant, *Paraponera clavata* (Hymenoptera: Formicidae). – Journal of the Kansas Entomological Society 61: 285-291.

Brown, W.L., Jr. & Kempf, W.W. 1968 [1967]: *Tatuidris*, a remarkable new genus of Formicidae (Hymenoptera). – Psyche 74: 183-190.

Cao, H., Boudinot, B.E., Wang, Z., Miao, X., Shih, C., Ren, D. & Gao, T. 2020: Two new iron maiden ants from Burmese amber (Hymenoptera: Formicidae: †Zigrasimeciini). – Myrmecological News 30: 161-173.

Carpenter, F.M. 1930: The fossil ants of North America. – Bulletin of the Museum of Comparative Zoology 70: 1-66.

Dejean, A. 1985: Étude éco-éthologique de la predation chez les fourmis du genre *Smithistruma* (Formicidae – Myrmicinae – Dacetini). II. Attraction des proies principals (Collemboles). – Insectes Socieux 32: 158-172.

Donoso, D.A. 2012: Additions to the taxonomy of the armadillo ants (Hymenoptera, Formicidae, *Tatuidris*). – Zootaxa 3503: 61-81.

Donoso, D.A. 2017: Capitulo 20. Subfamilia Agroecomyrmecinae. In: Fernández, F., Guerrero, R.J. & Delsinne, T. (Eds.): Hormigas de Colombia. – Universidad Nacional de Colombia, Bogotá, pp. 631-636.

Engelkes, K., Friedrich, F., Hammel, J.U. & Haas, A. 2018: A simple setup for episcopic microtomy and a digital image processing workflow to acquire high-quality volume data and 3D surface models of small vertebrates. – Zoomorphology 137: 213-228.

Ettershank, G. 1966: A generic revision of the world Myrmicinae related to *Solenopsis* and *Pheidologeton* (Hymenoptera: Formicidae). – Australian Journal of Zoology 14: 73-171.

Fisher, B.L. & Bolton, B. 2016: Ants of Africa and Madagascar: A Guide to the Genera. – University of California Press, Berkeley, CA, I-IX + 503 pp.

Gronenberg, W. 1995: The fast mandible strike in the trap-jaw ant *Odontomachus* I. Temporal properties and morphological characteristics. – Journal of Comparative Physiology A: Neuroethology, Sensory, Neural, and Behavioral Physiology 176: 391-398.

Gronenberg, W., Paul, J., Just, S. & Hölldobler, B. 1997: Mandible muscle fibers in ants: fast or powerful? – Cell and Tissue Research 289: 347-361.

Harris, R.A. 1979: A glossary of surface sculpturing. – Occasional Papers in Entomology 28: 1-31.

Hita-Garcia, F., Lieberman, Z., Audisio, Z.L., Liu, C. & Economo, E.P. 2019: Revision of the highly specialized ant genus *Discothyrea* (Hymenoptera: Formicidae) in the Afrotropics with X-ray microtomography and 3D cybertaxonomy. – Insect Systematics and Diversity 3: art. 5.

Jacquemin, J., Delsinne, T., Maraun, M. & Leponce, M. 2014: Trophic ecology of the armadillo ant, *Tatuidris tatusia*, assessed by stable isotopes and behavioral observations. – Journal of Insect Science 14: art. 108.

Jacquemin, J., Delsinne, T., Maraun, M. & Leponce, M. 2018: Erratum to "Trophic ecology of the armadillo ant, *Tatuidris tatusia*, assessed by stable isotopes and behavioral observations". – Journal of Insect Science 18: art. 9.

Kaspari, M. & Yanoviak, S.P. 2009: Biogeochemistry and the structure of tropical brown food webs. – Ecology 90: 3342-3351.

Keller, R.A. 2011: A phylogenetic analysis of ant morphology (Hymenoptera: Formicidae) with special reference to the poneromorph subfamilies. – Bulletin of the American Museum of Natural History 355: 1-90.

Kempf, W.W. 1960: "*Phalacromyrmex*", a new ant genus from Southern Brazil (Hymenoptera, Formicidae). – Revista Brasileira de Biologia 20: 89-92.

Kubota, H., Yoshimura, J., Niitsu, S. & Shimizu, A. 2019: Morphology of the tentorium in the ant genus *Lasius* Fabricius (Hymenoptera: Formicidae). – Scientific Reports 9: art. 6722.

Lacau, S., Groc, S., Dejean, A., de Oliveira, M.L. & Delabie, J.H.C. 2012: *Tatuidris kapasi* sp. nov.: a new armadillo ant from French Guiana (Formicidae: Agroecomyrmecinae). – Psyche 2012: art. 926089.

Larabee, F.J., Gronenberg, W. & Suarez, A.V. 2017: Performance, morphology and control of power-amplified mandibles in the trap-jaw ant *Myrmoteras* (Hymenoptera: Formicidae). – Journal of Experimental Biology 220: 3062-3071.

Lieberman, Z.E., Billen, J., van de Kamp, T. & Boudinot, B.E. 2022: The ant abdomen: the skeletomuscular and soft tissue anatomy of *Amblyopone australis* workers (Hymenoptera: Formicidae). – Journal of Morphology 283: 693-770.

Longino, J.T. 2010: *Tatuidris* of Costa Rica. – <https://ants.biology.utah.edu/genera/tatuidris/home.html>, retrieved 24 October 2022.

Lösel, P.D., Van De Kamp, T., Jayme, A., Ershov, A., Faragó, T., Pichler, O., Tan Jerome, N., Aadepu, N., Bremer, S., Chilingaryan, S.A., Heethoff, M., Kopmann, A., Odar, J., Schmelzle, S., Zuber, M., Wittbrodt, J., Baumbach, T. & Heuveline, V. 2020: Introducing Biomedisa as an open-source online platform for biomedical image segmentation. – Nature Communications 11: art. 5577.

Michener, C.D. & Fraser, A. 1978: A comparative anatomical study of mandibular structure in bees. – The University of Kansas Science Bulletin 51: 463-482.

Moffett, M.W. 1986: Revision of the myrmicine genus *Acanthomyrmex* (Hymenoptera: Formicidae). – Bulletin of the Museum of Comparative Zoology 151: 55-89.

Moreau, C.S., Bell, C.D., Vila, R., Archibald, S.B. & Pierce, N.E. 2006: Phylogeny of the ants: diversification in the age of angiosperms. – Science 312: 101-104.

Peeters, C., Molet, M., Lin, C.C. & Billen, J. 2017: Evolution of cheaper workers in ants: a comparative study of exoskeleton thickness. – Biological Journal of the Linnean Society 121: 556-563.

Pie, M.R. & Feitosa, R.M. 2016: Relictual ant lineages (Hymenoptera: Formicidae) and their evolutionary implications. – Myrmecological News 22: 55-58.

Porto, D.S. & Almeida, E.A. 2019: A comparative study of the pharyngeal plate of Apoidea (Hymenoptera: Aculeata), with implications for the understanding of phylogenetic relationships of bees. – Arthropod Structure & Development 50: 64-77.

Prebus, M.M. 2021: Phylogenetic species delimitation in the ants of the *Temnothorax salvini* group (Hymenoptera: Formicidae): an integrative approach. – Systematic Entomology 46: 307-326.

Prentice, M.A. 1998: The comparative morphology and phylogeny of apoid wasps (Hymenoptera: Apoidea). – Unpublished PhD dissertation, University of California, Berkeley, 1439 pp.

Püffel, F., Pouget, A., Liu, X., Zuber, M., van de Kamp, T., Roces, F. & Labonte, D. 2021: Morphological determinants of bite force capacity in insects: a biomechanical analysis of polymorphic leaf-cutter ants. – Journal of the Royal Society, Interface 18: art. 20210424.

Rabeling, C., Brown, J.M. & Verhaagh, M. 2008: Newly discovered sister lineage sheds light on early ant evolution. – Proceedings of the National Academy of Sciences of the United States of America 105: 14913-14917.

Richter, A., Boudinot, B.E., Yamamoto, S., Katzke, J. & Beutel, R.G. 2022: The first reconstruction of the head anatomy of a Cretaceous insect, †*Gerontoformica gracilis* (Hymenoptera: Formicidae), and the early evolution of ants. – Insect Systematics & Diversity 6: art. 4.

Richter, A., Hita Garcia, F., Keller, R.A., Billen, J., Economo, E.P. & Beutel, R.G. 2020: Comparative analysis of worker head anatomy of *Formica* and *Brachyponera* (Hymenoptera: Formicidae). – Arthropod Systematics & Phylogeny 78: 133-170.

Richter, A., Hita Garcia, F., Keller, R.A., Billen, J., Katzke, J., Boudinot, B.E., Economo, E.O. & Beutel, R.G. 2021a: The head anatomy of *Protanilla lini* (Hymenoptera: Formicidae: Leptanillinae), with a hypothesis of their mandibular movement. – Myrmecological News 31: 85-114.

Richter, A., Keller, R.A., Rosumek, F.B., Economo, E.P., Hita Garcia, F. & Beutel, R.G. 2019: The cephalic anatomy of workers of the ant species *Wasmannia affinis* (Formicidae, Hymenoptera, Insecta) and its evolutionary implications. – Arthropod Structure & Development 49: 26-49.

Richter, A., Schoeters, E. & Billen, J. 2021b: Morphology and closing mechanism of the mandibular gland orifice in ants (Hymenoptera: Formicidae). – Journal of Morphology 282: 1127-1140.

Romiguier, J., Borowiec, M.L., Weyna, A., Helleu, Q., Loire, E., La Mendola, C., Rabeling, C., Fisher, B.L., Ward, P.S. & Keller, L. 2022: Ant phylogenomics reveals a natural selection hotspot preceding the origin of complex eusociality. – Current Biology 32: 2942-2947.

Schmidt, C.A. & Shattuck, S.O. 2014: The higher classification of the ant subfamily Ponerinae (Hymenoptera: Formicidae), with a review of ponerine ecology and behavior. – Zootaxa 3817: 1-242.

Schoeters, E. & Billen, J. 1996: The post-pharyngeal gland in *Dinoponera* ants (Hymenoptera: Formicidae): unusual morphology and changes during the secretory process. – International Journal of Insect Morphology and Embryology 25: 443-447.

Ward, P.S., Brady, S.G., Fisher, B.L. & Schultz, T.R. 2015: The evolution of myrmicine ants: phylogeny and biogeography of a hyperdiverse ant clade (Hymenoptera: Formicidae). – Systematic Entomology 40: 61-81.

Ward, P.S. & Branstetter, M.G. 2022: Species paraphyly and social parasitism: Phylogenomics, morphology, and geography clarify the evolution of the *Pseudomyrmex elongatulus* group (Hymenoptera: Formicidae), a Mesoamerican ant clade. – Insect Systematics & Diversity 6: art. 4.

Ward, P.S. & Fisher, B.L. 2016: Tales of dracula ants: the evolutionary history of the ant subfamily Amblyoponinae (Hymenoptera: Formicidae). – Systematic Entomology 41: 683-693.

Wheeler, W.M. 1915 [1914]: The ants of the Baltic Amber. – Schriften der Physikalisch-Ökonomischen Gesellschaft zu Königsberg 55: 1-142.

Williams, J.L., Zhang, Y.M., LaPolla, J.S., Schultz, T.R. & Lucky, A.R. 2022: Phylogenomic delimitation of morphologically cryptic species in globetrotting *Nylanderia* (Hymenoptera: Formicidae) species complexes. – Insect Systematics & Diversity 6: art. 10.

Wilson, E.O. 2003: *Pheidole* in the New World. A dominant, hyperdiverse ant genus. – Harvard University Press, Cambridge, MA, ix + 794 pp.

Wipfler, B., Machida, R., Müller, B. & Beutel, R.G. 2011: On the head morphology of Grylloblattodea (Insecta) and the systematic position of the order, with a new nomenclature for the head muscles of Dicondylia. – Systematic Entomology 36: 241-266.

Zachos, J., Pagani, M., Sloan, L., Thomas, E. & Billups, K. 2001: Trends, rhythms, and aberrations in global climate 65 Ma to present. – Science 292: 686-693.

Zhang, W., Li, M., Zheng, G., Guan, Z., Wu, J. & Wu, Z. 2020: Multifunctional mandibles of ants: variation in gripping behavior facilitated by specific microstructures and kinematics. – Journal of Insect Physiology 120: art. 103993.